

# **Similarity renormalization group evolution for deuteron electrodisintegration in pionless effective field theory**

**Renormierungsgruppenevolution des Deuteronaufbruchs in pionloser effektiver Feldtheorie**

Master-Thesis von Marc Thomas Schönborn

Tag der Einreichung:

1. Gutachten: Prof. Ph.D. Achim Schwenk
2. Gutachten: Dr. Sebastian König



TECHNISCHE  
UNIVERSITÄT  
DARMSTADT

Institut für Kernphysik  
Fachbereich Physik

Similarity renormalization group evolution for deuteron electrodisintegration in pionless effective field theory  
Renormierungsgruppenevolution des Deuteronaufbruchs in pionloser effektiver Feldtheorie

Vorgelegte Master-Thesis von Marc Thomas Schönborn

1. Gutachten: Prof. Ph.D. Achim Schwenk
2. Gutachten: Dr. Sebastian König

Tag der Einreichung:

---

## Abstract

---

Similarity renormalization group (SRG) methods are widely used to decouple high- from low-momentum physics via a series of unitary transformations. When applied to study knockout processes, these methods leave the cross section invariant, while the wave functions, current operator, and the general  $T$ -matrix are changed individually during the evolution. These effects of evolution on the different ingredients strongly depend on kinematics and the resolution scale  $\lambda$  of the SRG. We use pionless effective field theory (EFT) as a simple framework to explore the systematics behind the kinematical dependence of evolution effects. The low-energy region of pionless EFT is of special interest for us in order to investigate the correlation between final-state interactions and evolution effects. Motivated by previous work using phenomenological nuclear potentials, we choose the simplest nuclear knock-out process, deuteron electrodisintegration, as a controlled laboratory in order to avoid complications through initial and induced many-body operators.



---

## **Erklärung zur Abschlussarbeit gemäß § 22 Abs. 7 und § 23 Abs. 7 APB TU Darmstadt**

---

Hiermit versichere ich, Marc Thomas Schönborn, die vorliegende Master-Thesis gemäß § 22 Abs. 7 APB der TU Darmstadt ohne Hilfe Dritter und nur mit den angegebenen Quellen und Hilfsmitteln angefertigt zu haben. Alle Stellen, die Quellen entnommen wurden, sind als solche kenntlich gemacht worden. Diese Arbeit hat in gleicher oder ähnlicher Form noch keiner Prüfungsbehörde vorgelegen.

Mir ist bekannt, dass im Falle eines Plagiats (§38 Abs.2 APB) ein Täuschungsversuch vorliegt, der dazu führt, dass die Arbeit mit 5,0 bewertet und damit ein Prüfungsversuch verbraucht wird. Abschlussarbeiten dürfen nur einmal wiederholt werden.

Bei der abgegebenen Thesis stimmen die schriftliche und die zur Archivierung eingereichte elektronische Fassung gemäß § 23 Abs. 7 APB überein.

Bei einer Thesis des Fachbereichs Architektur entspricht die eingereichte elektronische Fassung dem vorgestellten Modell und den vorgelegten Plänen.

Darmstadt, den 3. Januar 2019

---

(M. Schönborn)



---

## Contents

---

<b>1 Motivation</b>	<b>7</b>
<b>2 Theoretical background</b>	<b>9</b>
2.1 Effective field theory . . . . .	9
2.1.1 Pionless effective field theory . . . . .	10
2.2 Similarity renormalization group . . . . .	12
2.3 Deuteron electrodisintegration . . . . .	16
2.3.1 Basic setup . . . . .	16
2.3.2 Cross section decomposition . . . . .	17
2.4 Impulse approximation and final-state interactions . . . . .	21
2.4.1 Review of previous work . . . . .	24
2.5 Numerical implementation . . . . .	26
2.5.1 Matrix products on Gaussian mesh . . . . .	26
2.5.2 Solving the SRG flow equations . . . . .	27
2.5.3 Solving the Lippmann-Schwinger equation . . . . .	27
2.6 Numerical treatment of the $\delta$ -distribution . . . . .	29
<b>3 Results for the SRG evolution</b>	<b>30</b>
3.1 Evolving the Hamiltonian . . . . .	30
3.2 Calculating the U-matrices . . . . .	32
<b>4 <math>f_L</math> at different kinematics</b>	<b>34</b>
4.1 The quasi-free ridge beyond pionless EFT . . . . .	35
4.1.1 Final-state interactions . . . . .	35
4.1.2 Evolution effects . . . . .	36
4.2 Evolution effects in the pionless regime . . . . .	39
4.2.1 At the the quasi-free ridge . . . . .	39
4.2.2 Close to the quasi-free ridge . . . . .	39
4.2.3 Far off the quasi-free ridge . . . . .	40
4.2.4 Evolution effects for different binding energies . . . . .	41
4.3 Final-state interactions in the pionless regime . . . . .	44
4.3.1 Variation of the binding energy . . . . .	44
<b>5 Summary and outlook</b>	<b>50</b>
<b>6 Appendix</b>	<b>52</b>
6.1 Matrix products . . . . .	52
<b>References</b>	<b>54</b>

---



---

## 1 Motivation

---

Resolution dependence is an important aspect in the description of nature. In some cases, it is sufficient to watch a process at limited resolution. This phenomenon is visualized in Fig. 1. Both images show Abraham Lincoln, but the left picture is put together of many small images. Thus, it shows more details than necessary, making it harder to recognize the relevant aspects. The picture on the right is at lower resolution, but one can still identify its essence. This basic concept is the underlying idea in the construction of effective field theories (EFTs).

The fundamental theory of the strong interaction is quantum chromodynamics (QCD), with its degrees of freedom being quarks and gluons. QCD is nonperturbative at long distances due to its running coupling constant  $\alpha_s(Q^2)$ , with  $\lim_{Q \rightarrow 0} \alpha_s(Q^2) \rightarrow \infty$ . Nevertheless, it is possible to use EFTs in order to describe the low-momentum part of the strong interaction [1]. For small  $Q \propto 1/\lambda$ , with  $\lambda$  denoting the De-Broglie wave length, quarks and gluons are not resolved, which allows us to change the degrees of freedom. In chiral EFT, every particle except for nucleons and pions is integrated out. For very small  $Q$ , even pions are not resolved, which then leads to the pionless EFT that we will use in this work.

The same idea of resolution dependence is used in the construction of similarity renormalization group (SRG). The SRG changes the theoretical resolution of a given interaction via a set of unitary transformations, i.e., it is used to decouple the high- from the low-momentum physics, leading to so-called "softened" interactions. Since the potential is strongly affected by the SRG, one question then is: How do we handle observables involving external probes when using these evolved interactions?

When changing the decoupling scale  $\lambda$  of the SRG, non-observables are not invariant independently. The Hamiltonian, wave functions, and the  $T$ -matrices change and generally all operators have to be evolved consistently along with the Hamiltonian. Nevertheless, since the SRG uses unitary transformations, low-momentum observables remain unchanged. This means that all these different ingredients have to combine in a way that the invariance of observables is achieved. One major goal of this work is to understand how this happens in detail, building upon previous work in this direction [3, 4].

There are several complications emerging when dealing with SRG-evolved Hamiltonians. The Hamiltonian will develop many-body components, even if the initial Hamiltonian only includes one- and two-body terms. At the same time, a one-body current will develop two- and many-body components. In order to avoid these complications, we choose our theoretical laboratory to be deuteron electrodisintegration. Deuteron electrodisintegration with only an initial one-body current is the cleanest knockout

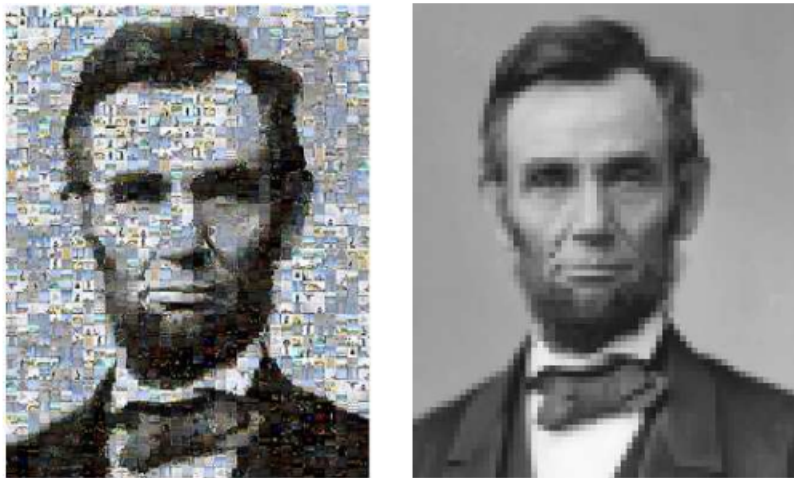


Figure 1: Two different pictures of Abraham Lincoln. The left picture is put together of many small images, showing more details than necessary. The right picture is at poor resolution, but one can still identify the important aspects. This illustrates the idea of effective field theories and renormalization group methods, where limited resolution is turned into an advantage (taken from Ref. [2]).

---

process and theoretically [5] as well as experimentally [6] well understood. Since there are only two nucleons involved, we do not have to consider any many-body components. However, there is still a lot to investigate: (i) how does the SRG-evolved deuteron wave function affect observables; (ii) what is the impact of final-state interactions (the interactions of the nucleons after the deuteron broke up) at certain resolutions and kinematics regarding the  $T$ -matrix; and (iii) how strong are the effects of induced two-body currents?

Investigating this using the Argonne  $v_{18}$  potential, More et al. [3] found that the effects of (i)-(iii) strongly depend on kinematics in a systematic way. One of the central results was that there is a correlation between evolution effects and final-state interactions. Furthermore, there is some particular regime of kinematic where both effects are almost negligible, and it is called the quasi-free ridge. Up to this date, the quasi-free ridge for deuteron electrodisintegration has only been investigated in the high-momentum area [3, 4]. One important question will be: does this correlation also exist in the low-momentum regime?

One important aspect when investigating this regime is the on-shell  $T$ -matrix describing the final-state scattering. For small momenta, the  $T$ -matrix is directly connected to the unnaturally large scattering length  $a_T = 5.4 \text{ fm}^{-1}$  of the  ${}^3\text{S}_1$  channel. The second important question of this work therefore is: is the quasi-free ridge really quasi-free in the low-momentum area, do the effects of the scattering length dominate, or is there some different contribution which we do not know yet?

Using pionless EFT allows a very simple treatment of this process, avoiding, for example, complications arising from the nuclear tensor force. In pionless EFT the only degrees of freedom are nucleons that interact via contact interactions. Since pions are integrated out, pionless EFT is valid in the low-momentum regime up to momenta smaller than the pion mass  $m_\pi \approx 140 \text{ MeV}$ . Christlmeier and Grießhammer [7] have shown that deuteron electrodisintegration can be described within this theory. Therefore, it is perfectly suited for our investigations.

This thesis is organized as follows. In Sec. II, we give the theoretical background on pionless EFT, similarity renormalization group, and deuteron electrodisintegration. In this part, we derive the formulas necessary to investigate the invariance of the cross section. In Sec. III, we present results for the evolved pionless potential and deuteron wave function as well as the transformation matrices. In Sec. IV, we show the results for the longitudinal structure function for different kinematics, giving answers to the questions stated above. Finally, in Sec. V we summarize our results and give an outlook on what can be done in future work.

## 2 Theoretical background

### 2.1 Effective field theory

The concept of effective field theories was pioneered by Weinberg in Ref. [8]. His idea was that a quantum field theory has no essential content other than analyticity, unitarity, cluster decomposition, and symmetry. The basic procedure in constructing an effective field theory includes three steps. (1) One has to choose the degrees of freedom that are suitable for the energy scale to investigate. In nuclear physics, instead of quarks and gluons, one chooses nucleons and pions. (2) Construct the most general Lagrangian consistent with the demands above (symmetry, unitarity etc.). (3) One has to order the infinitely many terms of the Lagrangian to estimate the importance of each term. This is called "power counting". The terms contributing the most are called leading order (LO), then next-to-leading order (NLO) and so on.

An analogy for effective field theories from classic electrodynamics is the multipole expansion. The potential at some position  $\mathbf{R}$  for a given charge density  $\rho(\mathbf{r})$  is given by

$$V(\mathbf{R}) = \int d^3r \frac{\rho(\mathbf{r})}{|\mathbf{R} - \mathbf{r}|}. \quad (1)$$

We can expand the integrand in a Taylor series,

$$\frac{1}{|\mathbf{R} - \mathbf{r}|} = \frac{1}{R} + r_i \frac{R_i}{R^3} + \mathcal{O}\left(\frac{1}{R^3}\right), \quad (2)$$

and plug this into Eq. (1), which leads to

$$\begin{aligned} V(\mathbf{R}) &= \frac{1}{R} \underbrace{\int d^3r \rho(\mathbf{r})}_{\text{charge } q} + \frac{R_i}{R^3} \underbrace{\int d^3r \rho(\mathbf{r}) r_i}_{\text{dipole moment } P_i} + \mathcal{O}\left(\frac{1}{R^3}\right) \\ &= \frac{q}{R} + \underbrace{\frac{1}{R^3} r_i P_i}_{\propto \frac{a}{R^2}} + \mathcal{O}\left(\frac{1}{R^3}\right). \end{aligned} \quad (3)$$

Compared to the first term, the second one is suppressed by a factor of  $a/R$ . This means that the series converges quickly for  $a \ll R$ . The huge advantage is that we do not need  $\rho(\mathbf{r})$  to calculate the potential, but we can fit  $q$ ,  $\mathbf{P}$  and so on to data. For a more detailed calculation, see Ref. [10].

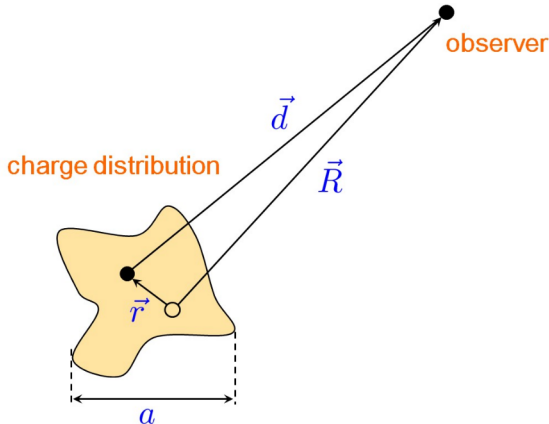


Figure 2: Visualization of the idea of effective field theories. For  $a \ll R$ , details of the charge distribution do not matter [9].

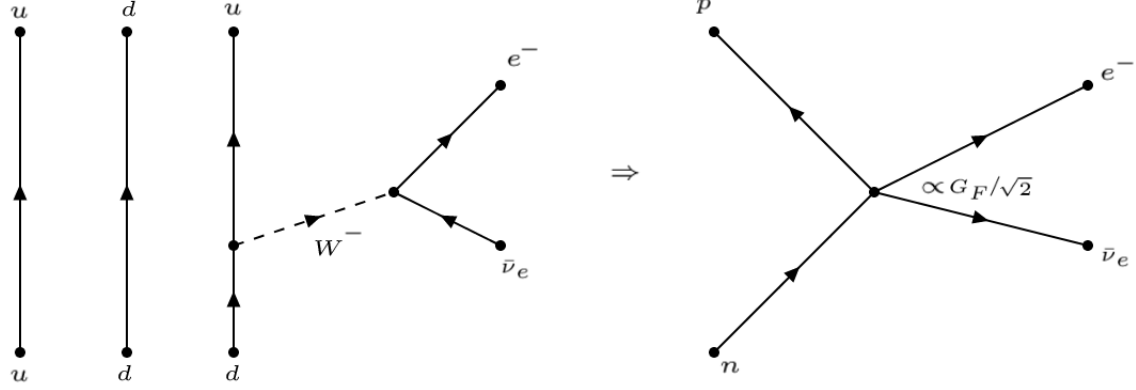


Figure 3: Fermi’s theory as an effective field theory to standard model.

Another example is Fermi’s theory of weak interaction. Today we know that the beta decay is mediated by the exchange of a charged  $W$  boson, which decays into an electron and a neutrino. From the standard model, this process is

$$\mathcal{M} \propto \frac{e^2}{8 \sin \theta_W} \frac{1}{M_W^2 - \mathbf{q}^2} = \underbrace{\frac{e^2}{8 \sin \theta_W M_W^2}}_{G_F/\sqrt{2}} \left[ 1 + \frac{\mathbf{q}^2}{M_W^2} + \dots \right], \quad (4)$$

where  $M_W = 80$  GeV is the  $W$  boson mass,  $\theta_W$  is the Weinberg angle, and  $\mathbf{q}$  is the momentum transfer. Since typical momentum transfers are  $|\mathbf{q}| = 1$  MeV, corrections to Fermi’s theory, which describes this process as a contact interaction, are  $\frac{q^2}{M_W^2} = \left(\frac{1}{80000}\right)^2$ . For more on the basic idea of effective field theories see e.g. Ref. [11] and Ref. [12].

### 2.1.1 Pionless effective field theory

We now give a brief overview on pionless EFT. In pionless EFT, pions as degrees of freedom are integrated out. The only degrees of freedom are nucleons, i.e., protons and neutrons [13]. Nucleons can only interact via contact interactions, which are delta-peak potentials and derivatives thereof in configuration space. Since all relative momenta are small in the regime where pionless EFT is used, a non-relativistic description is appropriate. Thus, effects like particles propagating backwards in time are negligible.

The effective Lagrangian defining pionless EFT is given by

$$\mathcal{L} = N^\dagger \left( i\partial_0 + \frac{\nabla^2}{2M} + \dots \right) N - C_T (N^\dagger P_t N)^2 - C_S (N^\dagger P_s N)^2 + \dots, \quad (5)$$

with the operators

$$\begin{aligned} P_t^i &= \frac{1}{\sqrt{8}} \sigma_2 \sigma^i \tau_2, \\ P_s^A &= \frac{1}{\sqrt{8}} \tau_2 \tau^A \sigma_2, \end{aligned} \quad (6)$$

where the pauli matrices  $\sigma$  and  $\tau$  are acting in spin space and isospin space, respectively, and  $N$  is the nonrelativistic nucleon field [14]. The first term of the Lagrangian is connected to the Schrödinger operator  $\mathcal{D} = i\partial_0 + \frac{\nabla^2}{2M}$ . By using the Euler-Lagrange equation for this term one directly arrives at the Schrödinger equation. The second and third terms are  $S$ -wave interactions, taking into account that a system of two nucleons with zero angular momentum can either exist in a spin singlet ( ${}^1S_0$ ) or a in a

spin triplet ( ${}^3S_1$ ). Therefore, there are two independent interactions in the Lagrangian. The  $C_S$  and  $C_T$  denote the low energy constants (LECs), which determine the strength of the contact interaction in these channels. The projection operators  $P_s^A$  and  $P_t^i$  project out the  ${}^1S_0$  and  ${}^3S_1$  partial waves. The ellipses in the Lagrangian stand for terms that are not at leading order or not at the two-body level.

Naturally, since pions are integrated out, pionless EFT is limited to momentum scales below the pion mass  $m_\pi = 140$  MeV. Nevertheless it has several applications and is particularly useful to describe low-energy processes. As an example, pionless EFT was used to calculate the deuteron electric form factors [15].

By construction, pionless EFT reproduces the effective range expansion

$$k \cot \delta_0(k) = -\frac{1}{a_S} + \frac{1}{2} r_e k^2 + \dots, \quad (7)$$

in order to fix the LECs. In nucleon-nucleon scattering, the scattering amplitude can be written in terms of the effective range,

$$T = -\frac{2\pi}{\mu} \frac{1}{k \cot \delta_0(k) - ik} = -\frac{2\pi}{\mu} \frac{1}{-\frac{1}{a_S} + \frac{1}{2} r_e k^2 + \dots - ik}. \quad (8)$$

The diagrams contributing to the scattering amplitude are shown in Fig. 4. Here, every vertex contributes with a contact interaction  $C_0$  given by

$$C_0({}^1S_0) = C_S, \quad (9)$$

$$C_0({}^3S_1) = C_T, \quad (10)$$

while every loop contributes as an integral,

$$I(E, \Lambda) = \int_0^\Lambda dq q^2 \frac{1}{E - \frac{q^2}{M} + i\epsilon} = \frac{\mu}{2\pi} \left( -\frac{2}{\pi} \Lambda - \underbrace{i\sqrt{2\mu E}}_{=ik} + \mathcal{O}\left(\frac{k^2}{\Lambda}\right) \right). \quad (11)$$

The potential here is regularized with a sharp cutoff. Without regularization, the integral is linearly divergent, which is obvious if one just counts the powers of momenta in the integrand. The scattering amplitude is then given by (see Fig. 4)

$$T = C_0 + C_0(IC_0) + C_0(IC_0IC_0) + \dots \quad (12)$$

Using Eq. (11), we arrive at a geometric series which converges to

$$T = \frac{1}{\frac{1}{C_0(\Lambda)} - \frac{\mu}{2\pi} \left( \frac{2}{\pi} \Lambda - ik + \mathcal{O}\left(\frac{k^2}{\Lambda}\right) \right)} \quad (13)$$

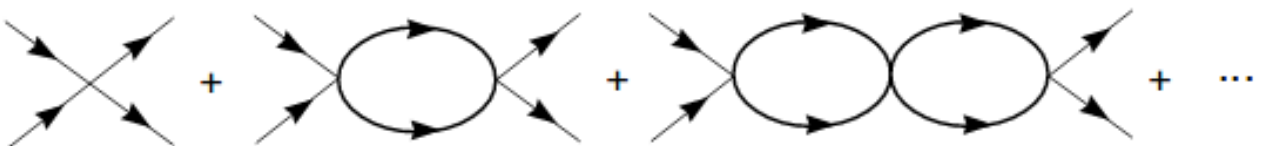


Figure 4: Diagrams contributing to the NN scattering amplitude. Every vertex contributes as a contact interaction  $C_0$  (taken from Ref. [16]).

and therefore reproduces the first term of the effective range expansion from Eq. (7). The renormalized contact interaction depends explicitly on the cutoff and is then given by

$$C_0(\Lambda) = \frac{2\mu}{\pi} \frac{1}{\frac{1}{a_S} - \frac{2}{\pi}\Lambda}. \quad (14)$$

For more on pionless EFT, see e.g. Ref. [17].

Christlmeier and Grießhammer [7] showed that pionless EFT is also very well suited to describe deuteron electrodisintegration, where they were not only able to reproduce the full triple differential cross section, but could also describe the different deuteron structure functions.

In this work, in contrast to the example above, we do not choose a Heaviside function as our regulator but a Gaussian regulator in order to cut off high momenta. So our potential is given by

$$V(k, k') = C_0 e^{\frac{-k^2 - k'^2}{\Lambda^2}}. \quad (15)$$

The deuteron is in the  ${}^3S_1$  channel which means that our contact interaction strength is  $C_0 = C_T$ .

## 2.2 Similarity renormalization group

The idea of renormalization group (RG) was developed by Kenneth Wilson. Studying phase transitions he found that scale dependence is an essential part of physics and that basically every theory is defined with a cutoff [18–20]. This idea was extended by Glazek and Wilson [21, 22] who presented a way to convert an arbitrary Hamiltonian into a band-diagonal Hamiltonian via unitary transformation in order to avoid ultra violet divergences in perturbation theory. Independently, an alternative formulation was found by Wegner [23] for condensed matter applications under the name "flow equations". Both formulations were proved to be equivalent [24].

In nuclear systems, RG methods are used in order to soften nuclear interactions. The goal is to decouple high- from low-momentum physics while leaving low-momentum observables unchanged. In Fig. 5 we show schematically two options for how the RG can be used to decouple a Hamiltonian. The  $V_{\text{low } k}$  method (left) lowers the cutoff  $\Lambda$  in small steps while requiring that for instance the on-shell  $T$ -matrix is invariant. The latter condition is used to adjust the low-momentum matrix elements.

The approach we use and want to investigate is the similarity renormalization group shown on the right in Fig. 5. The SRG achieves this decoupling by evolving the Hamiltonian via a series of infinitesimal,

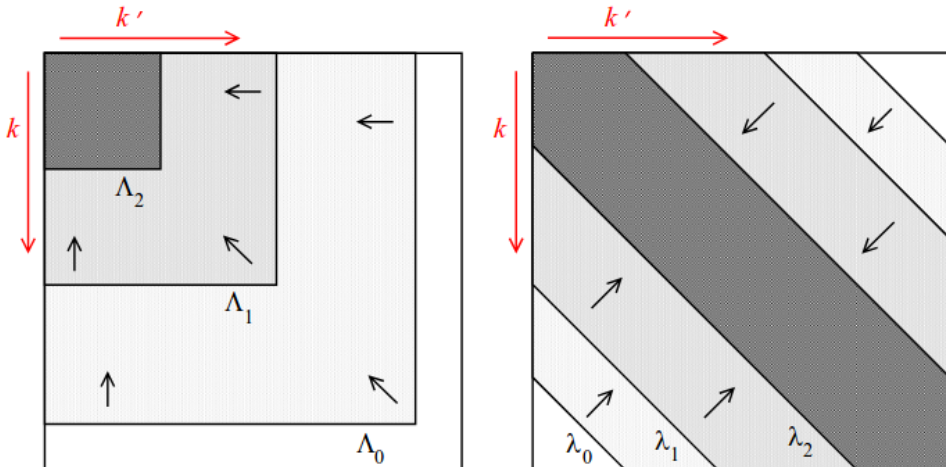


Figure 5: (Left) Schematic  $V_{\text{low } k}$  RG evolution with a sharp regulator and (right) SRG evolution (taken from [25]).

unitary transformations  $U_s$ , driving it to band-diagonal form. The evolved Hamiltonian then is given by [26]

$$H_s = U_s H_{s=0} U_s^\dagger, \quad (16)$$

with  $s$  being the flow parameter. Differentiating this with respect to  $s$ , we find

$$\frac{dH_s}{ds} = \frac{dU_s^\dagger}{ds} H_{s=0} U_s + U_s^\dagger H_{s=0} \frac{dU_s}{ds}. \quad (17)$$

The transformation matrices are unitary, i.e.  $U_s U_s^\dagger = U_s^\dagger U_s = \mathbb{1}$ , so we find that

$$0 = \frac{d}{ds}(U_s^\dagger U_s) = \frac{dU_s^\dagger}{ds} U_s + U_s^\dagger \frac{dU_s}{ds}. \quad (18)$$

Plugging this into Eq. (17) then leads to

$$\begin{aligned} \frac{dH_s}{ds} &= \frac{dU_s^\dagger}{ds} U_s U_s^\dagger H_{s=0} U_s + U_s^\dagger H_{s=0} U_s U_s^\dagger \frac{dU_s}{ds} \\ &= \frac{dU_s^\dagger}{ds} U_s U_s^\dagger H_{s=0} U_s - U_s^\dagger H_{s=0} U_s \frac{dU_s^\dagger}{ds} U_s \\ &= [\eta_s, H_s], \end{aligned} \quad (19)$$

where  $\eta_s$  is an arbitrary anti-Hermitian operator related to the transformation matrices via

$$\eta_s = \frac{dU_s}{ds} U_s^\dagger = -U_s^\dagger \frac{dU_s}{ds}. \quad (20)$$

It is convenient to choose  $\eta_s = M^2[G_s, H_s]$  with a Hermitian generator  $G_s$ . One common choice for the generator is the kinetic energy  $G_s = T$  [27] in order to suppress the Hamiltonian's off-diagonal elements in momentum space. Alternatives are for example  $G_s = T^2$  [28] or the diagonal part of the Hamiltonian  $G_s = \text{diag}(H_s)$  as advocated by Wegner [23]. Wegner's choice can be understood very intuitively. If the Hamiltonian commutes with its diagonal part, i.e.  $\eta_s = [\text{diag}(H_s), H_s] = 0$ , then the evolution has reached a fixed point.

The practical advantage of the SRG is that it extends computational possibilities. In particular, the convergence of methods using basis expansion like coupled cluster and in-medium SRG is improved [29–31]. This is shown in Fig. 6, where the triton binding energy is calculated in a harmonic oscillator basis for  $NN$ -interactions only for different values of  $\lambda = s^{-1/4}$ . The further one evolves, the faster the binding energy converges as a function of the model-space dimension.

For observables other than binding energies, it is not sufficient to simply evolve the Hamiltonian, every operator has to be evolved consistently along with the Hamiltonian. The flow equation for the operators is given by the same expression as for the Hamiltonian,

$$\frac{d\hat{O}_s}{ds} = [\eta_s, \hat{O}_s], \quad (21)$$

with the evolved operator  $\hat{O}_s$  defined as

$$\hat{O}_s = U_s \hat{O}_{s=0} U_s^\dagger. \quad (22)$$

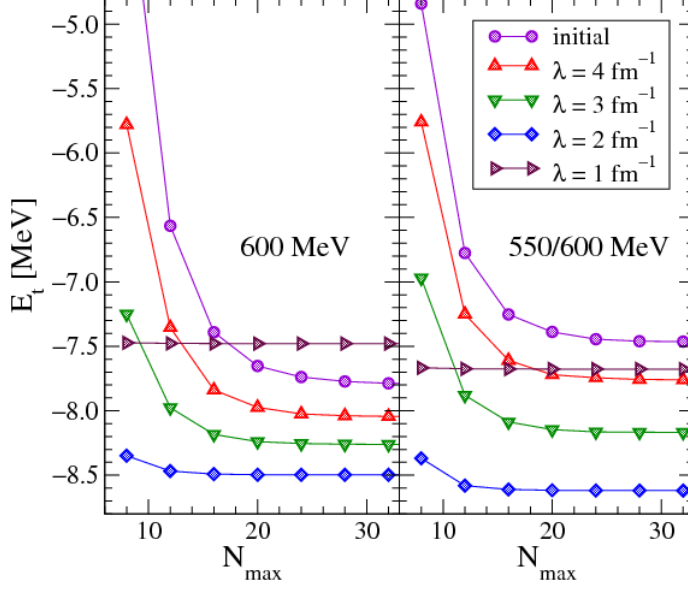


Figure 6: Triton binding energy for different values of the decoupling scale  $\lambda$  as a function of  $N_{max}$  in a harmonic oscillator basis [32].

Taking  $G_s = T$ , we now derive the flow equations, starting with those for the Hamiltonian itself. By using Eq. (19), we find

$$\begin{aligned} \frac{dH_s}{ds} &= M^2 [[T, H_s], H_s] \\ &= M^2 [T, H_s] H_s - M^2 H_s [T, H_s] \\ &= M^2 \left( 2TV_s T - TTV_s - V_s TT + TV_s V_s + V_s V_s T - 2V_s TV_s \right), \end{aligned} \quad (23)$$

where we used  $H_s = T + V_s$  in the last step. The kinetic energy does not evolve under the SRG by construction, so Eq. (23) reduces to a differential equation for  $V_s$ . We project this equation onto a partial-wave momentum basis by inserting  $\mathbb{1} = \frac{2}{\pi} \int dq q^2 |q\rangle \langle q|$  and calculate the different terms. For example, the first term in Eq. (23) gives:

$$\begin{aligned} 2 \langle k | TVT | k' \rangle &= 2 \int dq dq' \left( \frac{2}{\pi} \right)^2 q^2 q'^2 \langle k | T | q \rangle \langle q | V | q' \rangle \langle q' | T | k' \rangle \\ &= 2 \int dq dq' \left( \frac{2}{\pi} \right)^2 q^2 q'^2 \frac{k^2}{2\mu} \langle k | q \rangle V(q', q) \frac{q'^2}{2\mu} \langle q' | k' \rangle \\ &= 2 \int dq dq' \left( \frac{2}{\pi} \right)^2 q^2 q'^2 \frac{q'^2}{2\mu} \frac{k^2}{2\mu} \frac{\pi}{2q^2} \delta(k - q) \frac{\pi}{2q'^2} \delta(q' - k') V(q, q') \\ &= 2 \frac{k^2}{2\mu} \frac{k'^2}{2\mu} V(k, k'). \end{aligned} \quad (24)$$

Carrying out similar steps for all six terms, we arrive at

$$\begin{aligned} \frac{dV_s(k, k')}{ds} &= -(k^2 - k'^2)^2 V_s(k, k') \\ &\quad + \frac{2M}{\pi} \int_0^\infty dq q^2 (k^2 + k'^2 - 2q^2) V_s(k, q) V_s(q, k'), \end{aligned} \quad (25)$$

with  $\hbar = c = 1$  and  $M = 2\mu$ . In the limit where the first term dominates, i.e., for sufficiently small off-diagonal  $k$  and  $k'$ , the differential equation is given by

$$\frac{dV_s(k, k')}{ds} \approx -(k^2 - k'^2)^2 V_s(k, k'), \quad (26)$$

which has the solution [33]

$$V_s(k, k') \approx e^{-s(k^2 - k'^2)^2} V_{s=0}(k, k') = e^{-(k^2 - k'^2)^2 / \lambda^4} V_{\lambda=\infty}(k, k'). \quad (27)$$

As mentioned above, it is possible to switch from flow parameter  $s$  to  $\lambda = s^{-1/4}$ , which has units of  $\text{fm}^{-1}$  [34]. The motivation for this change of variables is that  $\lambda$  then is a measure of the band-diagonal width of  $V_\lambda$  as shown in Eq. (27).

Since we want to investigate observables other than energies, we need a flow equation for operators. Therefore, we project Eq. (21) onto the partial-wave momentum basis, giving

$$\frac{dO_s(k, k')}{ds} = \frac{2M}{\pi} \int dq q^2 [(k^2 - q^2)V_s(k, q)O_s(q, k') + (k'^2 - q^2)O_s(k, q)V_s(q, k')], \quad (28)$$

where the same steps were used as in Eq. (24). In practice, it is more efficient not to solve Eq. (28), but to instead construct the transformation matrices  $U_s(k, k')$ . There are two possibilities to calculate them. The first one is via the eigenvectors of the evolved and unevolved Hamiltonian,

$$U_s(k, k') = \sum_{\alpha} \langle k | \psi_{\alpha}(s) \rangle \langle \psi_{\alpha}(0) | k' \rangle. \quad (29)$$

The second possibility is to derive a flow equation for the transformation matrices. In order to do so, we use Eq. (20) and multiply it with  $U_s$  from the right (using  $U_s^\dagger U_s = \mathbb{1}$ ), leading to

$$\begin{aligned} \frac{dU_s}{ds} &= M^2 [T, H_s] U_s \\ &= M^2 [TH_s U_s - H_s T U_s]. \end{aligned} \quad (30)$$

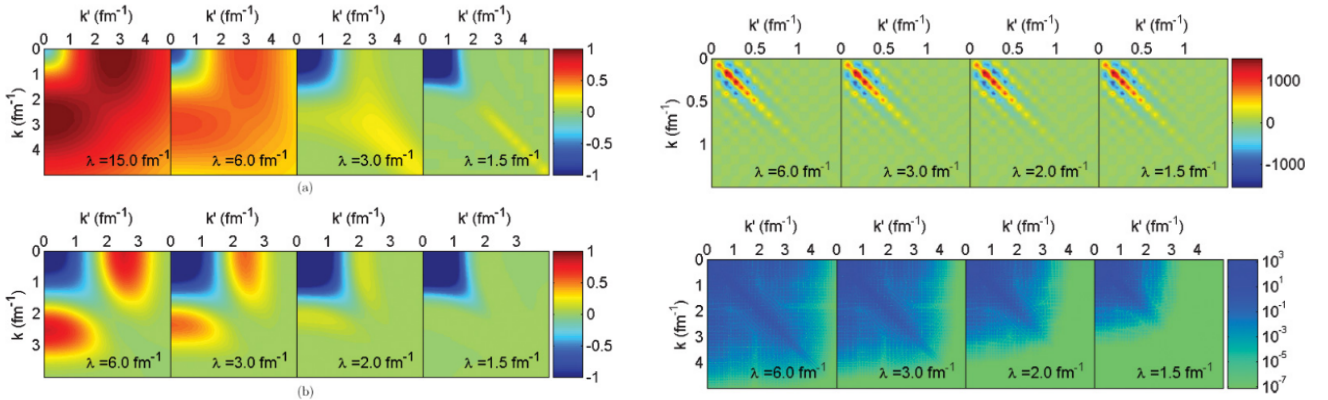


Figure 7: (Left) SRG evolution for (top) the Argonne  $v_{18}$  from  $\lambda = 15 \text{ fm}^{-1}$  to  $\lambda = 1.5 \text{ fm}^{-1}$  and for the (bottom) chiral  $N^3LO$  Entem and Machleidt potential with  $\Lambda = 500 \text{ MeV}$  from  $\lambda = 6 \text{ fm}^{-1}$  to  $\lambda = 1.5 \text{ fm}^{-1}$ . (Right) SRG evolution of the integrand of the deuteron quadrupole moment expectation value from  $\lambda = 6 \text{ fm}^{-1}$  to  $\lambda = 1.5 \text{ fm}^{-1}$  in a (top) linear and (bottom) logarithmic scale using the  $N^3LO$  EM 500-MeV potential [35].

Then, following the same steps as for the potential, i.e. projecting onto the partial-wave momentum basis, we arrive at the differential equation for the  $U$ -matrices,

$$\begin{aligned} \frac{dU_s(k, k')}{ds} &= M^2 \int dq q^2 dq' \left(\frac{2}{\pi}\right)^2 \left\{ \langle k | T | p \rangle \langle p | V | p' \rangle \langle p' | U | k' \rangle - \langle k | V | p \rangle \langle p | T | p' \rangle \langle p' | U | k' \rangle \right\} \\ &= \frac{2M}{\pi} \int dq q^2 (k^2 - q^2) V_s(k, q) U_s(q, k'). \end{aligned} \quad (31)$$

The evolved potential  $V_s$  appears in this equation, which means that we have to solve Eqs. (25) and (31) simultaneously. Some typical SRG evolutions for different potentials (left) as well as for the integrand of the deuteron quadrupole moment (right) [35] are shown in Fig. 7. As the potential is evolved to smaller values of  $\lambda$ , off-diagonal elements become more and more suppressed and the matrix is driven to band-diagonal form.

While changing the resolution, i.e., evolving to smaller values of  $\lambda$ , many-body forces are generated in the evolved Hamiltonian. To see this, it is instructive to write down the second-quantized Hamiltonian,

$$H_\lambda = \sum \langle T \rangle a^\dagger a + \sum \langle V_\lambda^{(2)} \rangle a^\dagger a^\dagger a a + \dots, \quad (32)$$

where indices are suppressed. The operators  $a^\dagger$  and  $a$  are creation and annihilation operators, respectively, in some single particle basis with respect to the vacuum. Plugging this into the flow equation, we find (schematically) [25]

$$\begin{aligned} \frac{dV_s}{ds} &= \left[ \left[ \underbrace{\sum_{G_s} a^\dagger a}_{G_s}, \underbrace{\sum_{\text{2-body}} a^\dagger a^\dagger a a}_{\text{2-body}} \right], \underbrace{\sum_{\text{2-body}} a^\dagger a^\dagger a a}_{\text{2-body}} \right] \\ &= \dots + \underbrace{\sum_{\text{3-body}} a^\dagger a^\dagger a^\dagger a a a}_{\text{3-body}} + \dots \end{aligned} \quad (33)$$

This shows that, even if the initial Hamiltonian has no many-body components, they arise naturally as a part of the SRG flow. These many-body forces become more and more relevant the further one evolves. This is shown in Fig. 6. Up to  $\lambda = 2 \text{ fm}^{-1}$ , the calculation converges to the correct value of the triton binding energy  $E_t = -8.482 \text{ MeV}$ . For  $\lambda = 1 \text{ fm}^{-1}$ , the numerical convergence is still improved. However, the calculation converges to an incorrect value for  $E_t$ . This happens due to the fact that the induced many-body components are omitted in the calculation. In general, up to  $A$ -body operators are induced by the SRG evolution. An  $A$ -body force is however only probed in an  $A$ -nucleon system. Truncating the SRG flow equations at the two-body level preserves the properties of the two-nucleon system, e.g., the deuteron binding energy. Truncations at the three-body level preserve properties of  $A = 3$  nuclei, and so on. However, truncating the flow equation at particle rank  $i$  in an  $A$ -body system (with  $A > i$ ) causes a violation of the exact unitarity which the SRG otherwise ensures by construction [36]. This leads to a resolution-scale dependence of many-body results (see e.g. Ref. [37]). Further insight into SRG and other renormalization group methods like the  $V_{\text{low } k}$  method can be gained from Ref. [32].

## 2.3 Deuteron electrodisintegration

### 2.3.1 Basic setup

In order to investigate the operator evolution and final-state interactions, we choose our theoretical laboratory to be deuteron electrodisintegration. This process is the simplest nucleon-knockout reaction and is theoretically as well as experimentally well understood. Because of the fact that only two nucleons are included in this process, i.e., a proton and a neutron, we do not have to take into account many-body ( $A > 2$ ) forces and currents, although, as explained above, these are generated by the SRG evolution. The

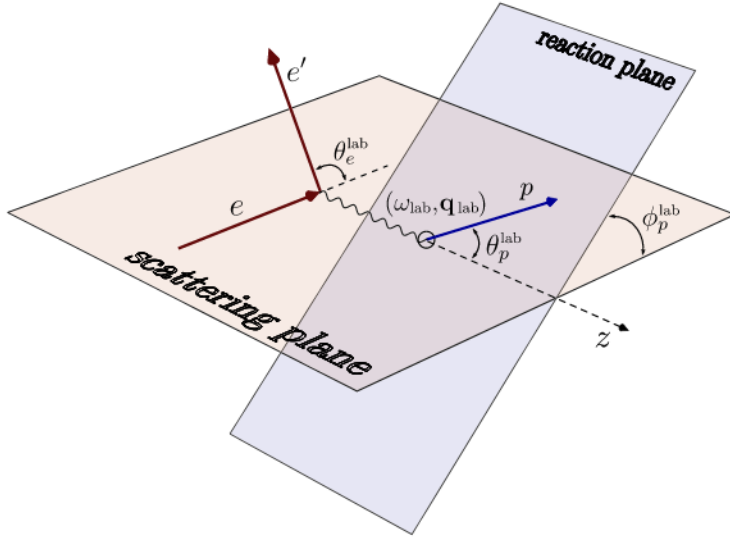


Figure 8: Kinematics of deuteron electrodisintegration. The electron transfers a virtual photon to the deuteron, having enough energy to break up the deuteron into a proton and a neutron. The scattering angle of the electron is  $\theta_e^{\text{lab}}$ . Meanwhile,  $\phi_p^{\text{lab}}$  is the angle between the scattering plane containing the electron momentum vectors and the reaction plane formed by the outgoing proton and neutron (taken from [3]).

kinematics of this process in the laboratory frame are shown in Fig. 8. The incoming electron transfers a virtual photon with four-momentum  $Q = (\omega, \mathbf{q})$ , which has enough energy to break up the deuteron into its components. The electron scattering angle is denoted by  $\theta_e^{\text{lab}}$ . The momentum of the outgoing proton (neutron) in the c.m. frame is  $\mathbf{p}' (-\mathbf{p}')$ , while both nucleons have the same energy  $E' = p'^2/M$ , with  $M$  denoting the average nucleon mass. The photons momentum is chosen to be along the  $z$ -axis and the angles of  $\mathbf{p}'$  relative to  $\mathbf{q}$  are denoted by  $\Omega_{p'} = (\Theta', \Phi')$ . The scattering plane is spanned by the incoming and outgoing electron momentum vectors and the reaction plane is formed by the outgoing proton and neutron momentum vectors. The angle between those two planes is denoted by  $\phi_p^{\text{lab}}$ .

### 2.3.2 Cross section decomposition

The triple differential cross section for this process is given by

$$\frac{d^3\sigma}{dk'^{\text{lab}} d\Omega_e^{\text{lab}} d\Omega_p^{\text{lab}}} = \frac{\alpha}{2\pi^2} \frac{k'^{\text{lab}}}{k^{\text{lab}}(Q^2)^2} \left[ v_L f_L + v_T f_T + v_{TT} f_{TT} \cos(2\phi_p^{\text{lab}}) + v_{LT} f_{LT} \cos(\phi_p^{\text{lab}}) \right], \quad (34)$$

where  $k^{\text{lab}}$  and  $k'^{\text{lab}}$  are the magnitude of the three-momenta of incoming and outgoing electron,  $\Omega_e^{\text{lab}}$  and  $\Omega_p^{\text{lab}}$  are the solid angles of electron and proton,  $Q^2$  is the four-momentum-squared of the photon, and  $\alpha$  is the fine structure constant. The  $v_i$  are electron kinematic factors and the  $f_i$  are the deuteron structure functions. These structure functions are directly related to the cross section and thus independent of the SRG scale  $\lambda$ .

We now derive a formula for the longitudinal structure function  $f_L$ , starting with the calculation for the cross section. The Feynman diagram for the one-photon exchange is shown in Fig. 9. We do not consider any many-photon exchanges because they are strongly suppressed. Cross sections are in general

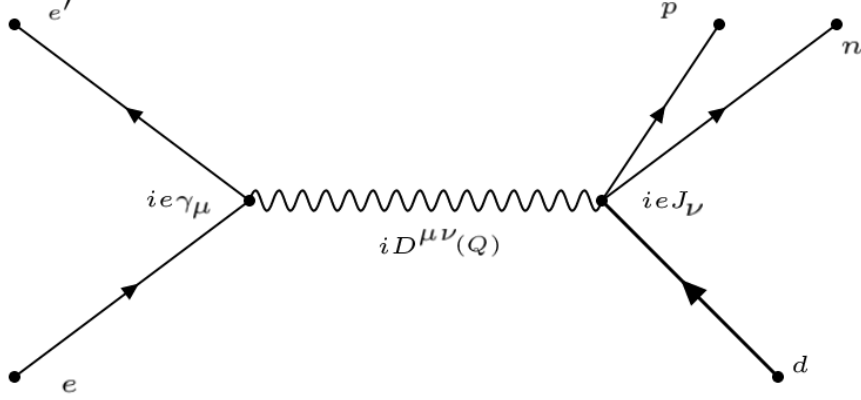


Figure 9: Feynman diagram for deuteron electrodisintegration. The incoming electron transfers a photon to the deuteron, which then is broken up into a neutron and a proton.

calculated via the invariant matrix element of the process,  $\mathcal{M}_{fi}$ , and some kinematic factors, i.e.

$$\begin{aligned} d\sigma &= \frac{1}{\beta} \frac{m_e^2 M_p M_n}{\epsilon \epsilon' E_p E_n} \sum_{i,f} \frac{d^3 k'}{(2\pi)^3} \frac{d^3 p_n}{(2\pi)^3} \frac{d^3 p_p}{(2\pi)^3} (2\pi)^4 \delta^{(4)}(K + P_d - K' - P_n - P_p) |\mathcal{M}_{fi}|^2 \\ &= \frac{m_e^2 M_p M_n}{k \epsilon' E_p E_n} (2\pi)^{-5} \sum_{i,f} |\mathcal{M}_{fi}|^2 k'^2 dk' p_p^2 dp_p d\Omega_e d\Omega_p \delta(\epsilon + M_d - \epsilon' - E_p - E_n) \end{aligned} \quad (35)$$

where  $K = (\epsilon, \mathbf{k})$ ,  $K' = (\epsilon', \mathbf{k}')$ ,  $P_d = (M_d, \mathbf{p}_d)$ , and  $P_p/P_n = (E_{p/n}, \mathbf{p}_{p/n})$  are the incoming and outgoing electron, deuteron and proton/neutron four-momenta in the laboratory system, respectively,  $Q = (\omega, \mathbf{q})$  is the photons four-momentum, and  $\beta = \frac{k'}{\epsilon}$  is the electrons velocity. Here,  $M_d = 2M + E_B$  is the deuteron mass and  $E_B$  its binding energy  $E_B = -2.225$  MeV.

The three-dimensional momentum-conserving part of the delta distribution has been canceled against the integral over the neutron momentum. The remaining energy conserving part of the delta distribution can be rewritten via

$$\delta(g(p_p)) = \sum_{p_0} \frac{\delta(p_p - p_0)}{|g'(p_0)|}, \quad (36)$$

with  $\{p_0\}$  being the zeros of the function  $g$ . In this case,  $g(p_p)$  is given by

$$g(p_p) = \epsilon + M_d - \underbrace{\epsilon'}_{=E_p} - \underbrace{\sqrt{p_p^2 + M_p^2}}_{=E_p} - \underbrace{\sqrt{(\mathbf{k} - \mathbf{k}' - \mathbf{p}_p)^2 + M_n^2}}_{=E_n}. \quad (37)$$

Using this in Eq. (35), the triple differential cross section can be written as

$$\frac{d^3 \sigma}{d\epsilon'^{\text{lab}} d\Omega_e^{\text{lab}} d\Omega_p^{\text{lab}}} = \frac{m_e^2 M_p M_n}{(2\pi)^5 M_d} \frac{k' p_p}{k} \sum_{i,f} |\mathcal{M}_{fi}|^2, \quad (38)$$

with the invariant matrix element given by

$$\begin{aligned} \mathcal{M}_{fi} &= \underbrace{\bar{u}(K', s') (-ie\gamma^\mu) u(K, s)}_{\text{leptonic current}} \times \underbrace{\frac{-ig^{\mu\nu}}{Q^2}}_{\text{photon propagator}} \times \underbrace{ieJ^\nu(\mathbf{q})_{if}}_{\text{hadronic current}} \\ &= -\frac{ie^2}{Q^2} \bar{u}(K', s') \gamma^\mu u(K, s) J_\mu(\mathbf{q})_{if}, \end{aligned} \quad (39)$$

where we used Feynman gauge, i.e.  $iD_F^{\mu\nu}(Q) = \frac{-ig^{\mu\nu}}{Q^2}$ . We now calculate the absolute value squared and take into account spin sums and averages, leading to

$$\sum_{s,s',i,f} |\mathcal{M}_{fi}|^2 = \frac{e^4}{(Q^2)^2} \frac{1}{4m_e^2} \text{Tr}[\gamma_\mu(\not{k}' + m_e)\gamma_\nu(\not{k} + m_e)] \sum_{i,f} (J^\mu(\mathbf{q}))_{if}^* J^\nu(\mathbf{q})_{if}, \quad (40)$$

where we applied the spin sums

$$\sum_s u(K, s) \bar{u}(K, s) = \frac{\not{k} + m_e}{2m_e}. \quad (41)$$

By using the standard trace rules for  $\gamma$ -matrices, i.e.,

$$\begin{aligned} \text{Tr}(\gamma^\mu \gamma^\nu) &= 4g^{\mu\nu}, \\ \text{Tr}(\underbrace{\gamma^\mu \dots \gamma^\rho}_{\text{odd}}) &= 0, \\ \text{Tr}(\gamma^\mu \gamma^\nu \gamma^\rho \gamma^\sigma) &= 4[g^{\mu\nu}g^{\rho\sigma} - g^{\mu\rho}g^{\nu\sigma} + g^{\mu\sigma}g^{\nu\rho}], \end{aligned}$$

we find

$$\sum_{i,f} |\mathcal{M}_{fi}|^2 = \frac{(4\pi\alpha)^2}{(Q^2)^2} \frac{1}{2m_e^2} \left[ K'_\mu K_\nu + K'_\nu K_\mu - \underbrace{(K \cdot K' - m_e^2)}_{=-\frac{1}{2}Q^2} g_{\mu\nu} \right] \sum_{i,f} \underbrace{(J^\mu)^*(\mathbf{q})_{if} J^\nu(\mathbf{q})_{if}}_{W(\mathbf{q})^{\mu\nu}}, \quad (42)$$

where we furthermore expressed the electron charge  $e$  in terms of the fine structure constant  $\alpha \approx \frac{1}{137}$ ,

$$e^2 = 4\pi\alpha. \quad (43)$$

Plugging this into the cross section gives us [38]

$$\frac{d^3\sigma}{d\epsilon'^{\text{lab}} d\Omega_e^{\text{lab}} d\Omega_p^{\text{lab}}} = \frac{\alpha^2 M_p M_n}{8\pi^3 M_d} \frac{k' p_p}{k(Q^2)^2} \mathcal{R}, \quad (44)$$

with

$$\mathcal{R} = \chi(K, K')_{\mu\nu} W^{\mu\nu}(\mathbf{q}), \quad \chi(K, K')_{\mu\nu} = 2[K_\mu K'_\nu + K'_\mu K_\nu] + Q^2 g_{\mu\nu}. \quad (45)$$

We can further evaluate  $\mathcal{R}$  and find

$$\mathcal{R} = |P_\mu J^\mu(q)_{if}|^2 + Q^2 J_{if}^*(q) J^\mu(q)_{if}, \quad (46)$$

where we used current conservation, i.e.  $P_\mu J^\mu = 2K_\mu J^\mu$  with  $P = K + K'$ . The vector part of the hadronic current,  $\mathbf{J}(\mathbf{q})_{if}$ , can be expressed in terms of the standard unit spherical vectors  $\mathbf{e}(\mathbf{q}; 1, m)$ ,

$$\mathbf{J}(\mathbf{q}) = \sum_{m=-1,0,1} J(\mathbf{q}; m)_{if} \mathbf{e}^*(\mathbf{q}; 1, m), \quad (47)$$

where  $m$  labels the different possible polarizations. We can plug this into Eq. (46) and find

$$\mathcal{R} = |P^0 \rho(\mathbf{q})_{if} - \sum_n J(\mathbf{q}, n)_{if} \mathbf{e}^*(\mathbf{q}; 1, n) \cdot \mathbf{P}|^2 + Q^2 \left[ |\rho(\mathbf{q})_{if}|^2 - \sum_{n,m} J(\mathbf{q}, n)_{if} \mathbf{e}^*(\mathbf{q}; 1, n) J^*(\mathbf{q}, m)_{if} \mathbf{e}(\mathbf{q}; 1, m) \right]. \quad (48)$$

From current conversation,

$$Q^0 J^0(\mathbf{q})_{if} - \mathbf{q} \cdot \mathbf{J}(\mathbf{q})_{if} = \omega \rho(\mathbf{q})_{if} - q J(\mathbf{q}; 0)_{if} = 0, \quad (49)$$

it follows that

$$J(\mathbf{q}; 0)_{if} = \frac{\omega}{q} \rho(\mathbf{q})_{if}, \quad (50)$$

with  $J^0(\mathbf{q})_{if} = \rho(\mathbf{q})_{if}$ . We can then write out the sums in Eq. (48) explicitly and replace  $J(\mathbf{q}; 0)_{if}$ , which leads to

$$\begin{aligned} \mathcal{R} = & |(\epsilon + \epsilon')\rho(\mathbf{q}) - J(\mathbf{q}, -1)\mathbf{e}^*(\mathbf{q}; 1, -1) \cdot \mathbf{P} - \frac{\omega}{q}\rho(\mathbf{q})\mathbf{e}^*(\mathbf{q}; 1, 0) \cdot \mathbf{P} - J(\mathbf{q}, +1)\mathbf{e}^*(\mathbf{q}; 1, +1) \cdot \mathbf{P}|^2 \\ & + Q^2 [ |\rho(\mathbf{q})|^2 - J(\mathbf{q}, -1)\mathbf{e}^*(\mathbf{q}; 1, -1)J^*(\mathbf{q}, -1)\mathbf{e}(\mathbf{q}; 1, -1) - J(\mathbf{q}, -1)\mathbf{e}^*(\mathbf{q}; 1, -1)\frac{\omega}{q}\rho(\mathbf{q})_{if}\mathbf{e}(\mathbf{q}; 1, 0) \\ & - J(\mathbf{q}, -1)\mathbf{e}^*(\mathbf{q}; 1, -1)J^*(\mathbf{q}, 1)\mathbf{e}(\mathbf{q}; 1, 1) - \dots ]. \end{aligned} \quad (51)$$

We are only interested in the longitudinal part in this work, which means we set  $n = m = 0$ . We then find that  $\mathcal{R}_L$ , defined as the sum of these terms, can be written as

$$\mathcal{R}_L = |\rho(q)|^2 \left[ (P_0 - \frac{\omega}{q}|P| \cos \theta_e)^2 + Q^2 \left( 1 - \frac{\omega^2}{q^2} \right) \right], \quad (52)$$

where we used that

$$\mathbf{P} \cdot \mathbf{e}^*(\mathbf{q}; 1, 0) = P_z = |P| \cos \theta_e. \quad (53)$$

Combining this with Eq. (44), we find that the longitudinal part of the cross section is given by [39]

$$\frac{d^3\sigma_L}{d\mathbf{k}_e^{\text{lab}} d\Omega_e^{\text{lab}} d\Omega_p^{\text{lab}}} = \underbrace{\frac{\alpha}{6\pi^2} \frac{k^{\text{lab}}}{k^{\text{lab}}(Q^2)^2}}_{v_0} \times \underbrace{12 \epsilon \epsilon' \left( \frac{Q^2}{\mathbf{q}^2} \right) \cos^2 \left( \frac{\theta_e}{2} \right)}_{v_L} \times \underbrace{\sum_{i,f} \Gamma_{i,f} \Gamma_{i,f}^*}_{f_L}, \quad (54)$$

with

$$\Gamma_{i,f} = -\pi \sqrt{2\alpha|\mathbf{p}'|E_p E_d / M_d} \langle \psi_f | \rho(\mathbf{q}) | \psi_i \rangle. \quad (55)$$

Here, we used that the quantities in the laboratory frame can be related to those in the c.m. frame by a Lorentz boost [7] with

$$\beta = \frac{|\mathbf{q}|^{\text{lab}}}{M_d + \omega^{\text{lab}}}, \quad \gamma = \frac{1}{\sqrt{1 - \beta^2}}, \quad (56)$$

i.e.,

$$\omega = \gamma \omega^{\text{lab}} - \beta \gamma q^{\text{lab}}, \quad |\mathbf{q}| = \beta \gamma M_d. \quad (57)$$

The energies are given in a relativistic fashion,  $E_p = \sqrt{M^2 + \mathbf{p}'^2}$  and  $E_d = \sqrt{M_d^2 + \mathbf{q}^2}$ . For a calculation taking all the polarization into account, see Ref. [38] and Ref. [40].

## 2.4 Impulse approximation and final-state interactions

In order to evaluate the matrix elements  $\langle \psi_f | \rho(\mathbf{q}) | \psi_i \rangle$  in Eq. (55) with SRG evolved operators and wave functions, we insert identities of the form  $U^\dagger U = \mathbb{1}$  into our expressions. The transformation matrix is not smooth at the diagonal. However, it is possible to split it into an identity and a residual, smooth matrix  $\tilde{U}$ , i.e.  $U = \mathbb{1} + \tilde{U}$ .

We distinguish in this work between impulse approximation and included final-state interactions. In the impulse approximation, the final-state of the nucleons is assumed to be a plane wave state, i.e.,

$$\langle \psi_f | \rho(\mathbf{q}) | \psi_i \rangle = \langle \phi | \rho(\mathbf{q}) | \psi_D \rangle . \quad (58)$$

Inserting identities as mentioned above, we can rewrite this expression as

$$\begin{aligned} \langle \phi | \rho(\mathbf{q}) | \psi_D \rangle &= \langle \phi | \underbrace{U^\dagger U}_{=1} \rho(\mathbf{q}) \underbrace{U^\dagger U}_{=1} | \psi_D \rangle \\ &= \langle \phi | (1 + \tilde{U}^\dagger) \rho^\lambda(\mathbf{q}) (1 + \tilde{U}) | \psi_D \rangle \\ &= \underbrace{\langle \phi | \tilde{U}^\dagger \rho^\lambda(\mathbf{q}) | \psi_D^\lambda \rangle}_A + \underbrace{\langle \phi | \rho^\lambda(\mathbf{q}) | \psi_D^\lambda \rangle}_B , \end{aligned} \quad (59)$$

with

$$\rho^\lambda(\mathbf{q}) = U \rho(\mathbf{q}) U^\dagger . \quad (60)$$

The one-body current is given by a momentum conserving delta distribution as

$$\begin{aligned} \langle \mathbf{k}_1 T_1 | \rho(\mathbf{q}) | \mathbf{k}_2 T_2 = 0 \rangle &= \frac{1}{2} \delta(\mathbf{k}_1 - \mathbf{k}_2 - \mathbf{q}/2) \\ &\quad + (-1)^{T_1} \frac{1}{2} \delta(\mathbf{k}_1 - \mathbf{k}_2 + \mathbf{q}/2) . \end{aligned} \quad (61)$$

Using Eq. (60), we can rewrite the expressions  $B$  and  $A$  from above as

$$\begin{aligned} \langle \phi | \rho^\lambda(\mathbf{q}) | \psi_D^\lambda \rangle &= \underbrace{\langle \phi | \tilde{U} \rho(\mathbf{q}) \tilde{U}^\dagger | \psi_D^\lambda \rangle}_{B_1} + \underbrace{\langle \phi | \tilde{U} \rho(\mathbf{q}) | \psi_D^\lambda \rangle}_{B_2} \\ &\quad + \underbrace{\langle \phi | \rho(\mathbf{q}) \tilde{U}^\dagger | \psi_D^\lambda \rangle}_{B_3} + \underbrace{\langle \phi | \rho(\mathbf{q}) | \psi_D^\lambda \rangle}_{B_4} , \end{aligned} \quad (62)$$

and

$$\begin{aligned} \langle \phi | \tilde{U}^\dagger \rho^\lambda(\mathbf{q}) | \psi_D^\lambda \rangle &= \underbrace{\langle \phi | \tilde{U}^\dagger \tilde{U} \rho(\mathbf{q}) \tilde{U}^\dagger | \psi_D^\lambda \rangle}_{A_1} + \underbrace{\langle \phi | \tilde{U}^\dagger \tilde{U} \rho(\mathbf{q}) | \psi_D^\lambda \rangle}_{A_2} \\ &\quad + \underbrace{\langle \phi | \tilde{U}^\dagger \rho(\mathbf{q}) \tilde{U}^\dagger | \psi_D^\lambda \rangle}_{A_3} + \underbrace{\langle \phi | \tilde{U}^\dagger \rho(\mathbf{q}) | \psi_D^\lambda \rangle}_{A_4} , \end{aligned} \quad (63)$$

respectively. It is obvious that the  $B_4$  term, using the unevolved deuteron wave function instead of the evolved one, is just the matrix element in the impulse approximation (see Eq. (59)).

We insert identities both in the partial-wave basis and in three-dimensional momentum space to evaluate these expressions. The normalization we use follows Landau [41], such that

$$\mathbb{1} = \frac{2}{\pi} \sum_{L,S,J,m_J,T} \int dp p^2 |p J m_J L S T\rangle \langle p J m_J L S T| , \quad \mathbb{1} = \int d^3 k |\mathbf{k}\rangle \langle \mathbf{k}| . \quad (64)$$

The overlap of two states is given by

$$\langle plm|\mathbf{k}\rangle = \sqrt{\frac{\pi}{2}} \frac{\delta(p-k)}{p^2} Y_{lm}^*(\Omega_{\mathbf{k}}). \quad (65)$$

The initial and final-state in deuteron electrodisintegration both have spin  $S = 1$ , so the outgoing plane-wave state in the partial-wave basis is given by [3]

$$\langle \phi | k_1 J_1 m_{J_1} L_1 S = 1 T_1 \rangle = \frac{1}{2} \sqrt{\frac{2}{\pi}} \frac{\delta(p' - k_1)}{k_1^2} C_{L_1 m_{J_1} - m_{s_f}, 1 m_{s_f}}^{J_1 m_{J_1}} (1 + (-1)^{T_1 + L_1}) Y_{L_1, m_{J_1} - m_{s_f}}(\theta', \phi'), \quad (66)$$

which in the case of  $L_1 = 0$  reduces to

$$\langle \phi | k_1 1 m_{s_f} 0 S = 10 \rangle = \frac{1}{\pi \sqrt{2}} \frac{\delta(p' - k_1)}{k_1^2}. \quad (67)$$

Since we work at leading order in pionless EFT, we only need to include  $L = 0$  here. Hence, also the transformation matrix and the wave function are limited to the  $S$ -wave level. This means that, for example, we have

$$\langle k_1 l_1 m_1 | \tilde{U} | k_2 l_2 m_2 \rangle = \tilde{U}(k_1, k_2) \delta_{l_1, 0} \delta_{l_2, 0} \delta_{m_1, 0} \delta_{m_2, 0}, \quad (68)$$

where we omitted the angular momentum  $J = 1$  and isospin  $T = 0$  which is due to  $|L - S| \leq J \leq |L + S|$  and the antisymmetry of the wave function, respectively. Using this, we derive the expression for  $B_1$ :

$$\begin{aligned} \langle \mathbf{p}' | \tilde{U} \rho^-(\mathbf{q}) \tilde{U}^\dagger | \psi_D^\lambda \rangle &= \left( \frac{2}{\pi} \right)^4 \sum \int dk_1 k_1^2 dk_2 k_2^2 dk_5 k_5^2 dk_6 k_6^2 d^3 k_3 d^3 k_4 \langle \mathbf{p}' | k_1 l_1 m_1 \rangle \langle k_1 l_1 m_1 | \tilde{U} | k_2 l_2 m_2 \rangle \\ &\quad \times \langle k_2 l_2 m_2 | \mathbf{k}_3 \rangle \langle \mathbf{k}_3 | \rho^-(\mathbf{q}) | \mathbf{k}_4 \rangle \langle \mathbf{k}_4 | k_5 l_5 m_5 \rangle \langle k_5 l_5 m_5 | \tilde{U}^\dagger | k_6 l_6 m_6 \rangle \langle k_6 l_6 m_6 | \psi_D^\lambda \rangle \\ &= \left( \frac{2}{\pi} \right)^4 \frac{1}{2} \sum \int dk_1 k_1^2 dk_2 k_2^2 dk_5 k_5^2 dk_6 k_6^2 d^3 k_3 \langle \mathbf{p}' | k_1 l_1 m_1 \rangle \langle k_1 l_1 m_1 | \tilde{U} | k_2 l_2 m_2 \rangle \\ &\quad \times \langle k_2 l_2 m_2 | \mathbf{k}_3 \rangle \langle \mathbf{k}_3 - \frac{\mathbf{q}}{2} | k_5 l_5 m_5 \rangle \langle k_5 l_5 m_5 | \tilde{U}^\dagger | k_6 l_6 m_6 \rangle \langle k_6 l_6 m_6 | \psi_D^\lambda \rangle \\ &= \left( \frac{2}{\pi} \right)^4 \frac{1}{2} \left( \frac{\pi}{2} \right)^{3/2} \sum \int dk_1 k_1^2 dk_2 k_2^2 dk_5 k_5^2 dk_6 k_6^2 d^3 k_3 \frac{\delta(p' - k_1)}{k_1^2} Y_{l_1, m_1} \\ &\quad \times (\Omega_{\mathbf{p}'}) \tilde{U}(k_1, k_2) \delta_{l_1, 0} \delta_{l_2, 0} \delta_{m_1, 0} \delta_{m_2, 0} \frac{\delta(k_2 - k_3)}{k_3^2} \frac{\delta(k_5 - |\mathbf{k}_3 - \frac{\mathbf{q}}{2}|)}{k_5^2} Y_{l_2, m_2}(\Omega_{\mathbf{k}_3}) \quad (69) \\ &\quad \times Y_{l_3, m_3}(\Omega_{\mathbf{k}_3 - \frac{\mathbf{q}}{2}}) \tilde{U}^\dagger(k_5, k_6) \delta_{l_5, 0} \delta_{l_6, 0} \delta_{m_5, 0} \delta_{m_6, 0} \psi_D^\lambda(k_6) \\ &= \frac{4}{\pi} \sqrt{\frac{2}{\pi}} (4\pi)^{-3/2} \int dk_6 k_6^2 dk_2 k_2^2 d \cos \theta_3 \tilde{U}(p', k_2) \tilde{U}^\dagger \left( \sqrt{k_2^2 - k_2 q \cos \theta_3 + \frac{q^2}{4}}, k_6 \right) \psi_D^\lambda(k_6). \end{aligned}$$

We restricted our derivation here to  $\rho^-(\mathbf{q})$ , which is defined as the first part of Eq. (61), since it can be shown that [3]

$$\langle \mathbf{p}' | \tilde{U} \rho(\mathbf{q}) \tilde{U}^\dagger | \psi_D^\lambda \rangle = 2 \langle \mathbf{p}' | \tilde{U} \rho^-(\mathbf{q}) \tilde{U}^\dagger | \psi_D^\lambda \rangle. \quad (70)$$

So we have

$$B_1 = \langle \mathbf{p}' | \tilde{U} \rho(\mathbf{q}) \tilde{U}^\dagger | \psi_D^\lambda \rangle = \frac{\sqrt{2}}{\pi^3} \int dk_6 k_6^2 dk_2 k_2^2 dx \tilde{U}(p', k_2) \tilde{U}^\dagger \left( \sqrt{k_2^2 - k_2 q x + \frac{q^2}{4}}, k_6 \right) \psi_D^\lambda(k_6). \quad (71)$$

The other expressions are given by:

$$B_2 = \frac{1}{\pi^2 \sqrt{2}} \int dk_2 k_2^2 dx \tilde{U}(p', k_2) \psi_D^\lambda \left( \sqrt{k_2^2 - k_2 q x + \frac{q^2}{4}} \right), \quad (72)$$

$$B_4 = \frac{1}{\pi \sqrt{2}} \psi_D^\lambda \left( \sqrt{p'^2 - p' q \cos \theta' + \frac{q^2}{4}} \right), \quad (73)$$

$$A_1 = \frac{\sqrt{8}}{\pi^4} \int dk_2 k_2^2 \tilde{U}(k_2, p') dk_3 k_3^2 \tilde{U}(k_2, k_3) dk_5 k_5^2 \psi_D^\lambda(k_5) dx \tilde{U} \left( k_5, \sqrt{k_3^2 - k_3 q x + \frac{q^2}{4}} \right), \quad (74)$$

$$A_2 = \frac{\sqrt{2}}{\pi^3} \int dk_2 k_2^2 \tilde{U}(k_2, p') dk_3 k_3^2 \tilde{U}(k_2, k_3) dx \psi_D^\lambda \left( \sqrt{k_3^2 - k_3 q x + \frac{q^2}{4}} \right), \quad (75)$$

$$A_3 = \frac{\sqrt{2}}{\pi^3} \int dk_6 k_6^2 dk_2 k_2^2 dx \tilde{U}^\dagger(p', k_2) \tilde{U}^\dagger \left( \sqrt{k_2^2 - k_2 q x + \frac{q^2}{4}}, k_6 \right) \psi_D^\lambda(k_6), \quad (76)$$

$$A_4 = \frac{1}{\pi^2 \sqrt{2}} \int dk_2 k_2^2 dx \tilde{U}^\dagger(p', k_2) \psi_D^\lambda \left( \sqrt{k_2^2 - k_2 q x + \frac{q^2}{4}} \right). \quad (77)$$

The  $B_3$  term has to be treated differently because, in theory, all partial waves contribute. Using Eq. (66) we find

$$\begin{aligned} B_3 &= \langle \mathbf{p}' | \rho(\mathbf{q}) \tilde{U}^\dagger | \psi_D^\lambda \rangle \\ &= 2 \sqrt{\frac{2}{\pi}} (4\pi)^{-1} \sum_{T_1=0,1} \sum_{L_1=0}^{L_{\max}} (1 + (-1)^{T_1+L_1}) Y_{L_1, m_{J_d} - m_{s_f}}(\theta', \phi') \sum_{J_1=|L_1-1|}^{L_1+1} C_{L_1 m_{J_d} - m_{s_f}, 1 m_{s_f}}^{J_1 m_{J_d}} C_{L_1 0, 1 m_{J_d}}^{* J_1 m_{J_d}} \\ &\quad \times \int dk_3 k_3^2 \psi_D^\lambda(k_3) dx P_{L_1}(x) \tilde{U} \left( k_3, \sqrt{p'^2 - p' q x + \frac{q^2}{4}} \right). \end{aligned} \quad (78)$$

From the calculation, however, we find that Eq. (78) converges for  $L_{\max} = 4$ .

Taking into account final-state interactions is achieved by carrying out similar steps. The final-state wave function with included final-state interactions is given by a plane wave state and a time-evolved plane wave, i.e.,

$$|\psi_f^{(\lambda)}\rangle = |\phi\rangle + G_0(E') T^{(\lambda)}(E') |\phi\rangle, \quad (79)$$

where  $G_0$  is the free two-nucleon propagator defined as

$$\langle k_1 | G_0^\dagger | k_2 \rangle = \frac{\pi}{2} \frac{\delta(k_1 - k_2)}{k_1^2} \frac{M}{p'^2 - k_1^2 - i\epsilon}. \quad (80)$$

In the case of the SRG-evolved final-state wave function, we have to replace the  $T$ -matrix in Eq. (79) by the SRG-evolved  $T$ -matrix  $T^\lambda$ , which is obtained by solving the LS-Equation for the SRG-evolved potential  $V_\lambda$  [3]. Using that, we have

$$\langle \psi_f^\lambda | \rho^\lambda(\mathbf{q}) | \psi_D^\lambda \rangle = \langle \phi | \rho^\lambda(\mathbf{q}) | \psi_D^\lambda \rangle + \langle \phi | T_\lambda^\dagger G_0^\dagger \rho^\lambda(\mathbf{q}) | \psi_D^\lambda \rangle. \quad (81)$$

The first term here is just the  $B$ -term defined above. For the second part we again use  $\rho^\lambda(\mathbf{q}) = U \rho(\mathbf{q}) U^\dagger$ . Separating the  $U$ -matrix into  $\mathbb{1} + \tilde{U}$  then leads to

$$\begin{aligned} \langle \phi | T_\lambda^\dagger G_0^\dagger \rho^\lambda(\mathbf{q}) | \psi_D^\lambda \rangle &= \underbrace{\langle \phi | T_\lambda^\dagger G_0^\dagger \tilde{U} \rho(\mathbf{q}) \tilde{U}^\dagger | \psi_D^\lambda \rangle}_{F_1} + \underbrace{\langle \phi | T_\lambda^\dagger G_0^\dagger \tilde{U} \rho(\mathbf{q}) | \psi_D^\lambda \rangle}_{F_2} \\ &\quad + \underbrace{\langle \phi | T_\lambda^\dagger G_0^\dagger \rho(\mathbf{q}) \tilde{U}^\dagger | \psi_D^\lambda \rangle}_{F_3} + \underbrace{\langle \phi | T_\lambda^\dagger G_0^\dagger \rho(\mathbf{q}) | \psi_D^\lambda \rangle}_{F_4}. \end{aligned} \quad (82)$$

In each of these terms, we have to restrict to  $L_1 = 0$ , coming here from the  $T$ -matrix acting only in the  $S$ -wave channels because the latter has the same restrictions as the potential itself. The different terms are then given by

$$\begin{aligned} F_1 &= \langle \mathbf{p}' | T_\lambda^\dagger G_0^\dagger \tilde{U} \rho(\mathbf{q}) \tilde{U}^\dagger | \psi_D^\lambda \rangle \\ &= \frac{16}{\pi^2} \sqrt{\frac{2}{\pi} \frac{M}{\hbar c}} (4\pi)^{-3/2} \int \frac{dk_2 k_2^2}{(p' + k_2)(p' - k_2 - i\epsilon)} T_\lambda^\dagger(p', k_2) dk_4 k_4^2 \tilde{U}(k_2, k_4) dk_6 k_6^2 dx \\ &\quad \times \tilde{U}^\dagger\left(\sqrt{k_4^2 - k_4 q x + \frac{q^2}{4}}, k_6\right) \psi_D^\lambda(k_6), \end{aligned} \quad (83)$$

$$\begin{aligned} F_2 &= \langle \mathbf{p}' | T_\lambda^\dagger G_0^\dagger \tilde{U} \rho(\mathbf{q}) | \psi_D^\lambda \rangle \\ &= \frac{8}{\pi} \sqrt{\frac{2}{\pi} \frac{M}{\hbar c}} (4\pi)^{-3/2} \int \frac{dk_2 k_2^2}{(p' + k_2)(p' - k_2 - i\epsilon)} T_\lambda^\dagger(p', k_2) dk_4 k_4^2 \\ &\quad \times \tilde{U}(k_2, k_4) dx \psi_D^\lambda\left(\sqrt{k_4^2 - k_4 q x + \frac{q^2}{4}}\right), \end{aligned} \quad (84)$$

$$\begin{aligned} F_3 &= \langle \mathbf{p}' | T_\lambda^\dagger G_0^\dagger \rho(\mathbf{q}) \tilde{U}^\dagger | \psi_D^\lambda \rangle \\ &= \frac{8}{\pi} \sqrt{\frac{2}{\pi} \frac{M}{\hbar c}} (4\pi)^{-3/2} \int \frac{dk_2 k_2^2}{(p' + k_2)(p' - k_2 - i\epsilon)} T_\lambda^\dagger(p', k_2) dk_4 k_4^2 dx \\ &\quad \times \tilde{U}^\dagger\left(\sqrt{k_2^2 - k_2 q x + \frac{q^2}{4}}, k_4\right) \psi_D^\lambda(k_4), \end{aligned} \quad (85)$$

$$\begin{aligned} F_4 &= \langle \mathbf{p}' | T_\lambda^\dagger G_0^\dagger \rho(\mathbf{q}) | \psi_D^\lambda \rangle \\ &= 4 \sqrt{\frac{2}{\pi} \frac{M}{\hbar c}} (4\pi)^{-3/2} \int \frac{dk_2 k_2^2}{(p' + k_2)(p' - k_2 - i\epsilon)} T_\lambda^\dagger(p', k_2) d\cos\theta \psi_D^\lambda\left(\sqrt{k_2^2 - k_2 q \cos\theta + \frac{q^2}{4}}\right). \end{aligned} \quad (86)$$

The  $F_4$  term with unevolved wave function and  $T$ -matrix represents the final-state interactions in the unevolved case, which is obvious from Eq. (79). Since we have to integrate over singularities in these expressions, we use the principle-value prescription. This is done for the  $T$ -matrix in Sec. 2.5.3 in order to solve the Lippmann-Schwinger equation and works analogously for  $F_1$ - $F_4$ .

#### 2.4.1 Review of previous work

The process of deuteron electrodisintegration has been studied with unitarily evolved potentials by More et al. [3] using the Argonne  $v_{18}$  potential. Some of their results are shown in Fig. 10, where the longitudinal structure function  $f_L$  is calculated for evolved and unevolved wave functions as well as for the evolved and unevolved operators as a function of  $\theta'$  for fixed kinematics.

It is obvious that the effects of SRG evolution and final-state interactions depend on the kinematics. For  $E' = 30$  MeV and  $q^2 = 16$  fm $^{-2}$  the structure function for the partly-evolved matrix elements differ strongly and only for the fully evolved matrix elements the structure function is equal to the unevolved result. In contrast to that, for  $E' = 100$  MeV and  $q^2 = 10$  fm $^{-2}$  there is no gap at all for all the different structure function calculations. These results are summarized in Fig. 11, where the influence of evolution effects and final-state interactions for different energies and momentum transfers is shown for  $\lambda = 1.5$  fm $^{-1}$ . The effects of evolution depend on kinematics in a systematic way. The black solid line is called quasi-free ridge or quasi-free kinematics. At this kinematics, final-state interactions are completely negligible, and the same has been found to be the case for evolution effects. The relation between nucleon energy and photon momentum is approximately  $E'$  (in MeV) =  $10 q^2$  (in fm $^{-2}$ ) for large  $q^2$ . Moving away from the quasi-free ridge, the influence of evolution effects becomes increasingly stronger.

The phenomenological explanation for final-state interactions not contributing at this kinematics is that the nucleons already are in their mass shell after the absorption of the photon due to  $\omega = 0$ . Therefore they are not necessary to "put" the nucleons on-shell. Since this argument is not satisfying, we use pionless effective field theory to investigate this topic further. The advantage of pionless EFT is that the expressions become very simple. This is due to the fact that the  $S - D$  mixing first enters pionless EFT at  $N^2LO$  via the S- to D-wave ratio [42]. Since we only take into account the leading order interaction, we thus can neglect the deuteron  $D$ -wave part.

We want to emphasize here that the results from above are obtained for large energies  $E'$ . The effects in the low-energy region, which is in particular the region of pionless EFT, have not been investigated. Therefore we can also investigate if the observations from More et al. hold under these conditions.

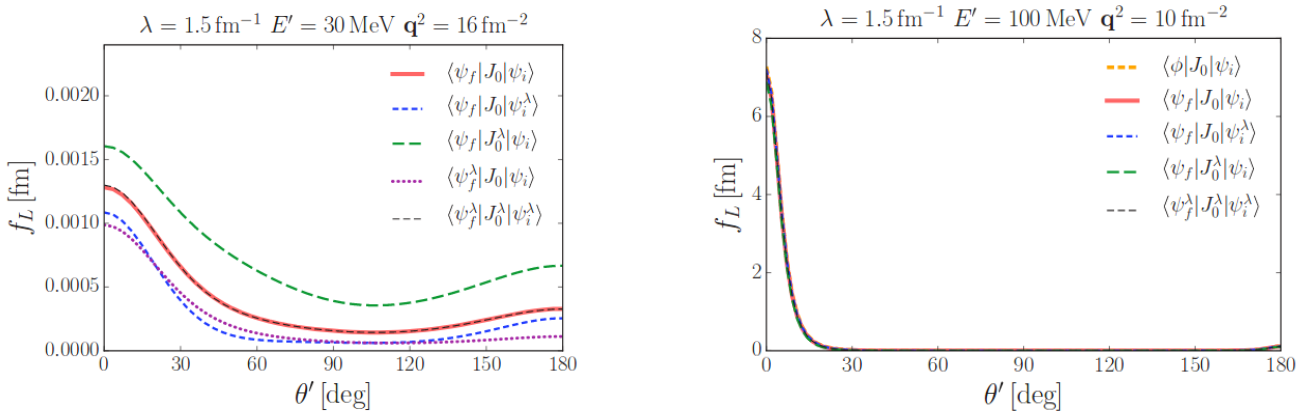


Figure 10: The longitudinal structure function  $f_L$  in two different types of kinematics combining un-evolved and evolved ( $\lambda = 1.5 \text{ fm}^{-1}$ ) states and operators. The calculations were done for (left)  $E' = 30 \text{ MeV}$  and  $q^2 = 16 \text{ fm}^{-2}$  and for (right)  $E' = 100 \text{ MeV}$  and  $q^2 = 10 \text{ fm}^{-2}$  [3].

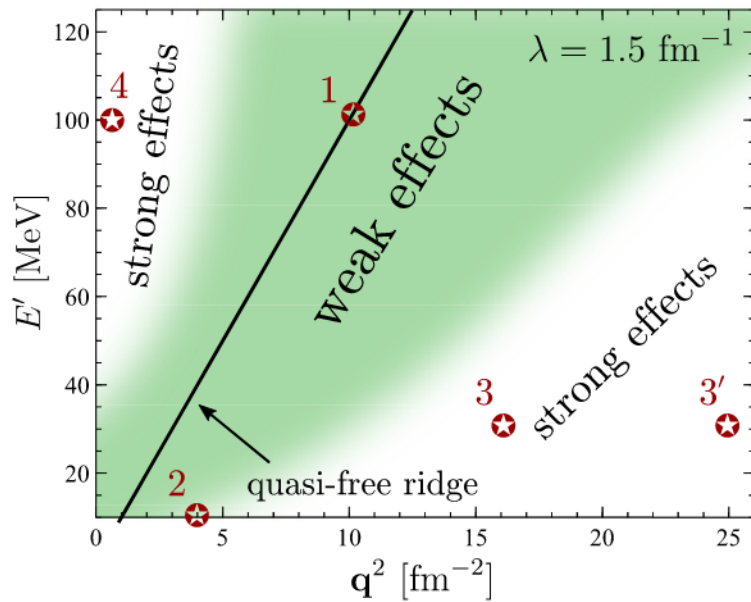


Figure 11: Effects of the SRG evolution and final-state interactions on the longitudinal structure function  $f_L$  for different kinematics evolved to  $\lambda = 1.5 \text{ fm}^{-1}$ . As one moves further away from the quasi-free ridge, the effects become progressively prominent. Results for the different spots are shown in Ref. [3].

## 2.5 Numerical implementation

In theory, momenta are continuous, meaning that operators like the potential  $V(k, k')$  are matrices of infinite size. However, it is possible evaluate these operators and certain values on a two-dimensional momentum grid. This is what we call a mesh.

### 2.5.1 Matrix products on Gaussian mesh

We solve our problem on a discretized Gaussian mesh with  $N$  Gauss-Legendre quadrature nodes  $\{p_i\}$  and weights  $\{w_i\}$ . In this work, we use exponentially weighted nodes and weights, given by

$$p_i = \exp(p'_i) - 1, \quad (87)$$

$$w_i = \exp(w'_i) \cdot p'_i, \quad (88)$$

where  $\{p'_i\}$  and  $\{w'_i\}$  are standard Gauss-Legendre weights and nodes, respectively. This has the advantage that the low-momentum part of integrals is taken into account stronger, leading to faster convergence in calculations. The identity, which includes an integral over all possible momenta, then changes to a sum over all mesh points, i.e.,

$$\mathbb{1} = \frac{2}{\pi} \int dq q^2 |q\rangle \langle q| \Rightarrow \frac{2}{\pi} \sum_i w_i p_i^2 |p_i\rangle \langle p_i|. \quad (89)$$

When calculating the matrix products, it is important to mind the conventions. Because of that, we show some of the matrix products that are often used in this work. We first look at the identity  $\mathbb{1}$ . Since we only look at the radial parts of the momentum, we have

$$\langle k_i | \mathbb{1} | k_j \rangle = \frac{\pi}{2} \frac{\delta_{ij}}{k_i k_j w_j}, \quad (90)$$

which is a discrete representation of the delta distribution. This can be constructed by looking at the wave function:

$$\begin{aligned} \langle k_i | \psi \rangle &= \langle k_i | \mathbb{1} | \psi \rangle \\ &= \frac{2}{\pi} \int dk' k'^2 \langle k_i | \mathbb{1} | k' \rangle \langle k' | \psi \rangle \\ &= \frac{2}{\pi} \sum_n w_n k_n^2 \langle k_i | \mathbb{1} | k_n \rangle \langle k_n | \psi \rangle \\ &= \frac{2}{\pi} \sum_n w_n k_n^2 \underbrace{\frac{\pi}{2} \frac{\delta_{in}}{k_i k_n w_n}}_{\langle k_i | \mathbb{1} | k_j \rangle} \psi(k_n) \\ &= \psi(k_i). \end{aligned} \quad (91)$$

This "identity matrix" automatically defines the starting point for our transformation matrices  $U_{s=0} = \frac{\pi}{2} \frac{\delta_{in}}{k_i k_n w_n}$ . Some of the shorter matrix products and matrix elements are given by

$$\langle k_i | V | k_j \rangle = V(k_i, k_j), \quad (92)$$

$$\langle k_i | T | k_j \rangle = \frac{\pi}{M} k_i^2 \frac{\delta_{ij}}{w_j k_i k_j}, \quad (93)$$

$$\langle k_i | H | \psi \rangle = \left[ \frac{k_i^2}{M} + \frac{2}{\pi} \sum_n w_n q_n^2 V(q_i, q_n) \right] \psi(q_n), \quad (94)$$

$$\langle k_i | U^\dagger U | \psi \rangle = \frac{4}{\pi^2} \sum_{n,m} w_n k_n^2 U^\dagger(k_i, k_n) w_m k_m^2 U(k_n, k_m) \psi(k_m), \quad (95)$$

which are all calculated by inserting one or more identities. The remaining, longer expressions for matrix products are shown in Appendix 5.1.

### 2.5.2 Solving the SRG flow equations

When solving the flow equations on a discretized mesh, Eq. (25) changes to

$$\begin{aligned} \frac{dV_s(k_i, k_j)}{ds} = & -(k_i^2 - k_j^2)^2 V_s(k_i, k_j) \\ & + \frac{2M}{\pi} \sum_{m=1}^N w_m k_m^2 (k_i^2 + k_j^2 - 2k_m^2) V_s(k_i, k_m) V_s(k_m, k_j). \end{aligned} \quad (96)$$

This is a simple matrix differential equation, which we solve numerically in GNU Octave. This has the advantage that it is very easy to work with vectors and matrices in this program. Solving the flow equation is then done as follows

1. Construct the right-hand side of Eq. (96) by multiplying the vectors of  $k$  and  $k'$  as line and column vectors, respectively, into the matrices  $V_s$ .
2. Reshape the resulting matrix into a vector of the length  $N^2$ .
3. Pass this vector into a differential equation solver (lsode, ode45, ...) with the boundary condition  $V_{s=0} = V_0$ .
4. Reshape the resulting vector into a  $N \times N$ -matrix.

By solving the Schroedinger equation for the (evolved) potential (see. Eq. (94)), which is done by diagonalization of the corresponding Hamiltonian, we get the spectrum and wave functions (as eigenvectors). The deuteron wave function is then given by the eigenvector corresponding to the only negative eigenvalue (bound state).

### 2.5.3 Solving the Lippmann-Schwinger equation

Since we need the  $T$ -matrix to calculate final-state interactions, we need to solve the Lippmann-Schwinger equation,

$$\langle \mathbf{p}' | t(E) | \mathbf{p} \rangle = \langle \mathbf{p}' | V | \mathbf{p} \rangle + \int d^3 p'' \langle \mathbf{p}' | V | \mathbf{p}'' \rangle \frac{1}{E - \mathbf{p}''^2/2m + i\epsilon} \langle \mathbf{p}'' | t(E) | \mathbf{p} \rangle. \quad (97)$$

We now sketch a method to calculate the half on-shell  $T$ -matrix, following the approach of Ref. [43]. We can write the LS equation in a simple form as

$$f(p) = g(p)h(p) + \int_0^{k_{\max}} dq K(p, q)f(q)h(q), \quad (98)$$

for some fixed momentum  $k$ ,  $f(p) = t(k, p)$ ,  $g(p) = g(k, p)$ , and  $K(p, q) = K(k, p, q)$ , which can be read off from Eq. (97). The function  $h(q)$  denotes the regulator we use and is in Eq. (97) included in the potential. For a sharp regulator, i.e.  $h(q) = \theta(\Lambda - q)$ ,  $k_{\max}$  then equals the cutoff  $\Lambda$ . In our case of a Gaussian regulator, we integrate to a maximum momentum  $k_{\max} = 3\Lambda$  to ensure that all high-momentum matrix elements of the potential go to zero. From this point on, the regulator is explicitly included in the potential again.

We first deal with the singularities. The kernel  $K(p, q)$  has a pole at  $q = q_0 + i\epsilon$ , so we rewrite the Lippmann-Schwinger equation as

$$f(p) = g(p) + \int_0^{k_{\max}} dq \frac{\tilde{K}(p, q)}{q - q_0 - i\epsilon} f(q), \quad (99)$$

with

$$\tilde{K}(p, q) = \begin{cases} (q - q_0) K(p, q), & q \neq q_0 \\ \lim_{q \rightarrow q_0} (q - q_0) K(p, q), & q = q_0 \end{cases}. \quad (100)$$

The residue can be obtained by a Laurent series for  $K$ . By using the Sokhotski–Plemelj theorem, which in a short version is given by

$$\frac{1}{x \pm i\epsilon} = \text{PV} \frac{1}{x} \mp i\pi\delta(x), \quad (101)$$

we get

$$f(p) = g(p) + \int_0^{k_{\max}} dq \frac{\tilde{K}(p, q)f(q) - \tilde{K}(p, q_0)f(q_0)}{q - q_0} + \tilde{K}(p, q_0)f(q_0) \left( i\pi + \text{PV} \int_0^{k_{\max}} \frac{dq}{q - q_0} \right). \quad (102)$$

The first integral no longer is a principal value integral, and the second integral can be carried out explicitly, leading to

$$\text{PV} \int_0^{k_{\max}} \frac{dq}{q - q_0} = \log \left( \frac{k_{\max} - q_0}{q_0} \right). \quad (103)$$

We solve this equation on the same mesh as the flow equations with momenta  $\{p_i\}$  and weights  $\{w_i\}$ . We then have  $p = p_i$ ,  $q = p_j$ ,  $g_i = g(p_i)$ ,  $f_i = f(p_i)$ , and  $\tilde{K}_{ij} = \tilde{K}(p_i, p_j)$ . The pole is included by setting  $p_{N+1} = q_0$ . Inserting this into Eq. (102), we find

$$\begin{aligned} f_i &= g_i + \sum_{j=1}^N w_j \frac{\tilde{K}_{ij} f_j - \tilde{K}_{iN+1} f_{N+1}}{p_j - p_{N+1}} + \tilde{K}_{iN+1} f_{N+1} \left( i\pi + \log \left( \frac{k_{\max} - p_{N+1}}{p_{N+1}} \right) \right) \\ &= g_i + \sum_{j=1}^N w_j K_{ij} f_j + \tilde{K}_{iN+1} f_{N+1} \left( i\pi + \log \left( \frac{k_{\max} - p_{N+1}}{p_{N+1}} \right) - \sum_{m=1}^N \frac{w_m}{p_m - p_{N+1}} \right). \end{aligned} \quad (104)$$

Note that  $\tilde{K}$  and the denominator have been combined to the original  $K$ . By setting  $i = N+1$ , we get the additional full on-shell equation

$$f_{N+1} = g_{N+1} + \sum_{j=1}^N w_j K_{N+1j} f_j + \tilde{K}_{N+1N+1} f_{N+1} \left( i\pi + \log \left( \frac{k_{\max} - p_{N+1}}{p_{N+1}} \right) - \sum_{m=1}^N \frac{w_m}{p_m - p_{N+1}} \right). \quad (105)$$

Combining Eq. (104) and Eq. (105), we finally arrive at

$$f_i = g_i + \sum_{j=1}^N A_{ij} f_j, \quad (106)$$

with

$$A_{ij} = \begin{cases} w_j K_{ij}, & j < N+1 \\ \tilde{K}_{ij} R, & j = N+1 \end{cases}, \quad \text{with } R = i\pi + \log \left( \frac{k_{\max} - p_{N+1}}{p_{N+1}} \right) - \sum_{m=1}^N \frac{w_m}{p_m - p_N}. \quad (107)$$

This is a simple matrix equation which can be easily solved by matrix inversion.

Theoretically, it is possible that one of the  $\{p_j\}$  equals  $q_0$ , such that we have a pole in Eq. (104). Fortunately, from a numerical point of view this is very unlikely to happen. However, if it happens, one can for example just change the number of mesh points in order to solve this problem.

---

## 2.6 Numerical treatment of the $\delta$ -distribution

---

The one-body current matrix element is basically given by a momentum conserving delta distribution. Hence, we have to evaluate the wave function and the transformation matrices at momenta like  $y = \sqrt{p'^2 - p'q \cos \theta + q^2/4}$  (see Eq. (73)) that are not on our mesh, making it necessary to interpolate these quantities. This is the reason why we separate  $U = \mathbb{1} + \tilde{U}$ , because  $\tilde{U}$  is amenable to interpolation. It is possible to express the latter as a vector product using splines. For the wave function, this leads to

$$\psi(p) = \sum_i^N S_i(p) \psi(p_i). \quad (108)$$

Here,  $S_i$  is the spline vector and  $\{p_i\}$  are the nodes of our mesh. For convenience, we can choose the same nodes for interpolation as we do for solving the flow equations. For a detailed derivation of  $S_i$ , see [44].

In this work, we have the more complicated case of three variables over which we have to integrate, all within one  $\delta$ -distribution. This is solved as

$$\int_0^{k_{\max}} dk_2 T(p', k_2) dk_3 \int_{-1}^1 dx \delta\left(k_3 - \sqrt{k_2^2 - k_2 q x + \frac{q^2}{4}}\right) \psi(k_3) = \sum_{i,j=1}^N \sum_{l=1}^M T(p', p_j) \omega_l \\ \times S_i\left(\sqrt{p_j^2 - p_j q x_l + \frac{q^2}{4}}\right) \psi(p_i), \quad (109)$$

where  $\{x_l\}$  and  $\{\omega_l\}$  are the Gauss-Legendre nodes and weights of the angular integration, respectively, and  $M$  is the size of this mesh. We treat the  $\delta$ -distribution as a three-dimensional spline tensor  $S_{ijl}$ . Thus, we can evaluate all the integrals as well as the interpolation as vector and matrix products (which are encoded in the sums). Since GNU Octave is very well suited to work with matrices and vectors, this calculation is done in a few seconds even for the relatively complicated expression  $F_1$  in which four integrals appear. In comparison to that, calculating the same expression in Mathematica by integrating over interpolated functions takes more than one hour.

### 3 Results for the SRG evolution

We now show some results for our solutions of the flow equations, i.e., the evolved potential, one-body current and the transformation matrices. We also show results for the deuteron wave function as well as for phase shifts that were calculated via the on-shell element of the unevolved (evolved)  $T$ -matrix  $T$  ( $T^\lambda$ ), verifying that observables are invariant.

#### 3.1 Evolving the Hamiltonian

We start with the LO pionless potential and its SRG evolution. The evolution is shown in Fig. 12 for the initial potential and three different values of  $\lambda$ . The potential is already very soft by construction, which is the reason why noticeable changes first appear at approximately  $\lambda = 3.5 \text{ fm}^{-1}$ . While evolving to smaller  $\lambda$ , the potential approaches the expected band-diagonal form. However, the band-diagonal form only appears at these values of  $\lambda$  due to the large cutoff  $\Lambda = 600 \text{ MeV}$ . For smaller cutoffs like  $\Lambda = 200 \text{ MeV}$ , one has to evolve to very small values  $\lambda$  in order to see a band-diagonal form. Thus, we can control the potential and its initial "softness" by regulating the cutoff and adjusting  $C_0$ . The fact that  $\lambda$  and  $\Lambda$  correlate is because both quantities are connected to the resolution. For a large cutoff  $\Lambda$  we are at good resolution. Hence, we have to evolve the potential to small  $\lambda$  in order to have limited resolution. Starting with a small cutoff, resolution is already limited such that we do not have to evolve to small  $\lambda$ .

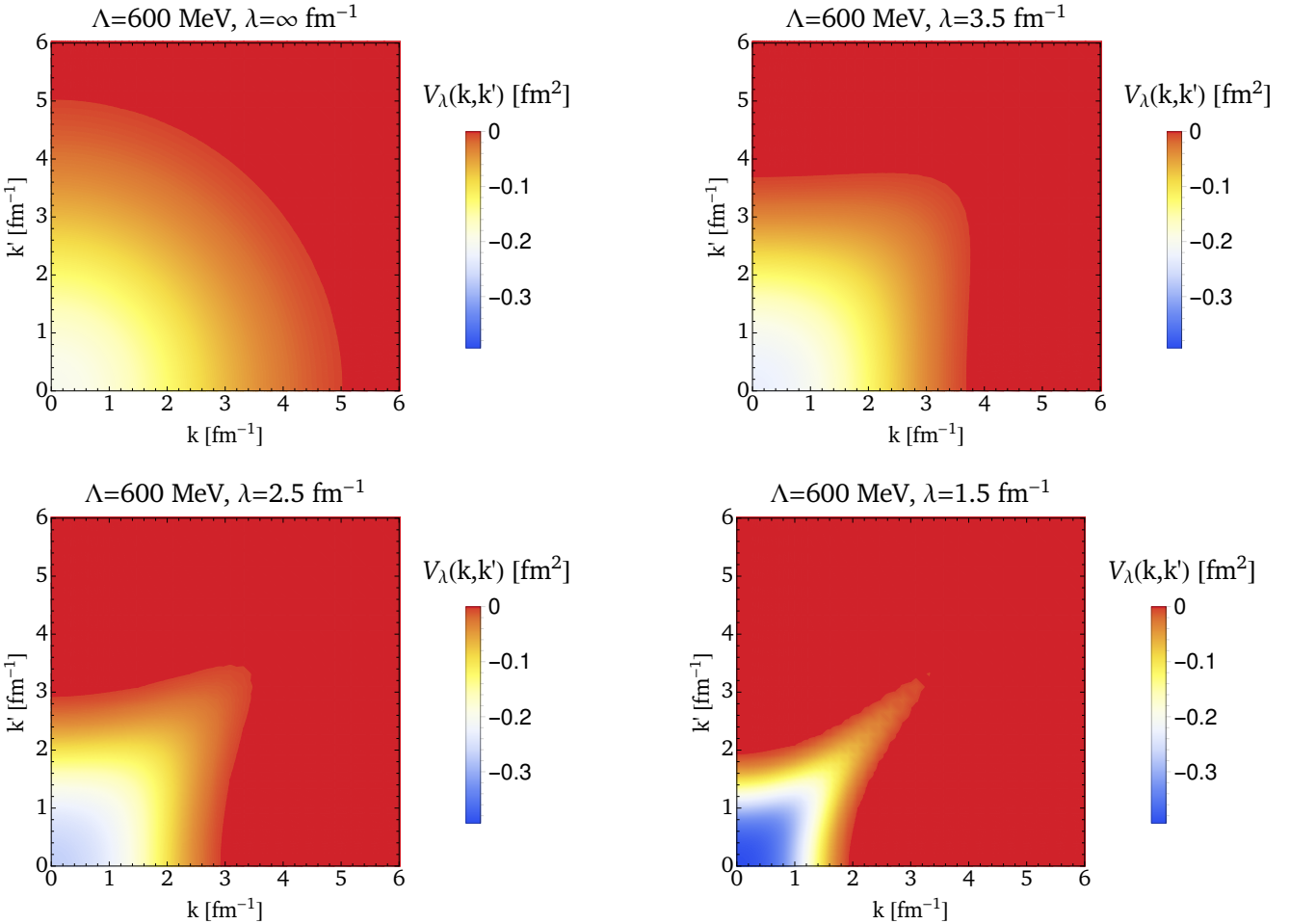


Figure 12: SRG evolution for the LO pionless EFT potential going from  $\lambda = \infty \text{ fm}^{-1}$  to  $\lambda = 1.5 \text{ fm}^{-1}$ . The potential is already very soft, which only leads to small changes during the evolution. However, for  $\lambda = 1.5 \text{ fm}^{-1}$  the band-diagonal form appears.

Since our goal is to calculate the longitudinal structure function, we also need the wave functions  $\psi$  and  $\psi^\lambda$ , which we either get by diagonalization of the Hamiltonian  $H$  and  $H_\lambda$ , respectively, or by using that the evolved wave function is obtained by acting with  $U_\lambda$  on the unevolved wave function, i.e., as  $U_\lambda |\psi_0\rangle = |\psi_\lambda\rangle$ . Figure 13 shows the deuteron wave function for different decoupling scales calculated via diagonalization (solid lines) and via applying the transformation matrices (symbols). We find perfect agreement for both methods, showing that they are equivalent. One can see that the wave function only changes in the high-momentum sector. This means that the SRG evolution effects only change the short-range (high-momentum) part of the wave function, while the long-range (low-momentum) part is invariant. It is also obvious that the difference to the unevolved wave function increases as  $\lambda$  is evolved to smaller values, consistent with the changes in the potential.

In order to include final-state interactions, we need the evolved  $T$ -matrix  $T^\lambda$ . More et al. [3] showed that  $T^\lambda$  is obtained by solving the Lippmann-Schwinger equation for the evolved potential  $V_\lambda$ . In order to test our results, we calculate observables. The on-shell element of the  $T$ -matrix is directly related to the phase shifts, which is an observable and therefore has to remain unchanged in the SRG evolution. We thus expect to see no difference for the phase shifts calculated for different  $\lambda$ . In Fig. 14 the phase shifts for  $\lambda = \infty \text{ fm}^{-1}$  and  $\lambda = 1.5 \text{ fm}^{-1}$  are shown as a function of the incoming/outgoing relative momentum  $k$ . We find that the phase shifts are indeed independent of  $\lambda$ . In addition to that, we find that the scattering length, which is also an observable and connected to the  $T$ -matrix, remains invariant under the SRG evolution. This observation confirms the correctness of our  $T$ -matrices and thus of our evolved potentials.

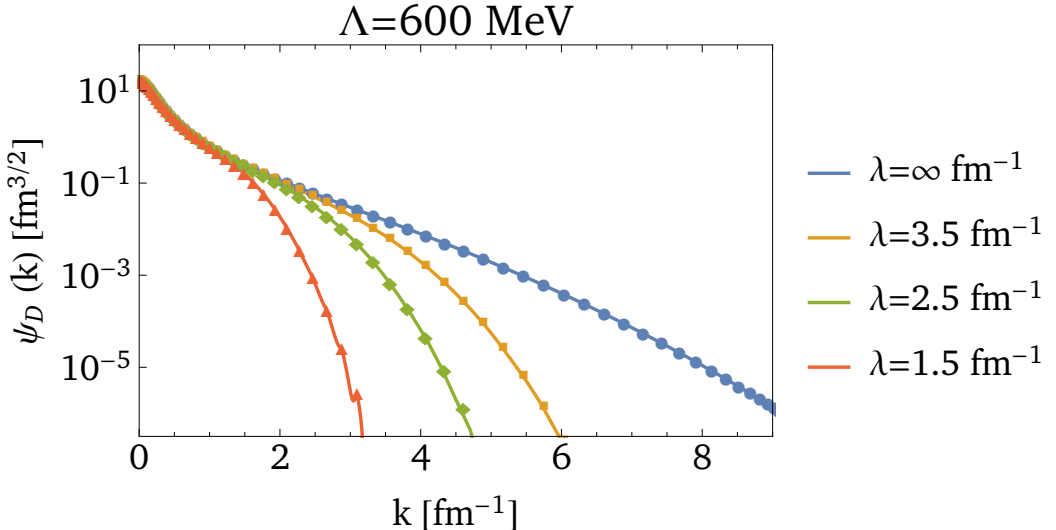


Figure 13: Deuteron wave functions for different values of  $\lambda$ , calculated via  $U|\psi_0\rangle = |\psi_s\rangle$  (symbols) and via diagonalization of the (evolved) Hamiltonian (solid lines). We find perfect agreement for both calculation methods. For small momenta all the wave functions are equal. For larger momenta, the wave functions differ and the differences compared to the unevolved wave function become larger as we evolve to smaller  $\lambda$ . This shows that the SRG evolution mainly changes the short-range (high-momentum) part of the wave function.

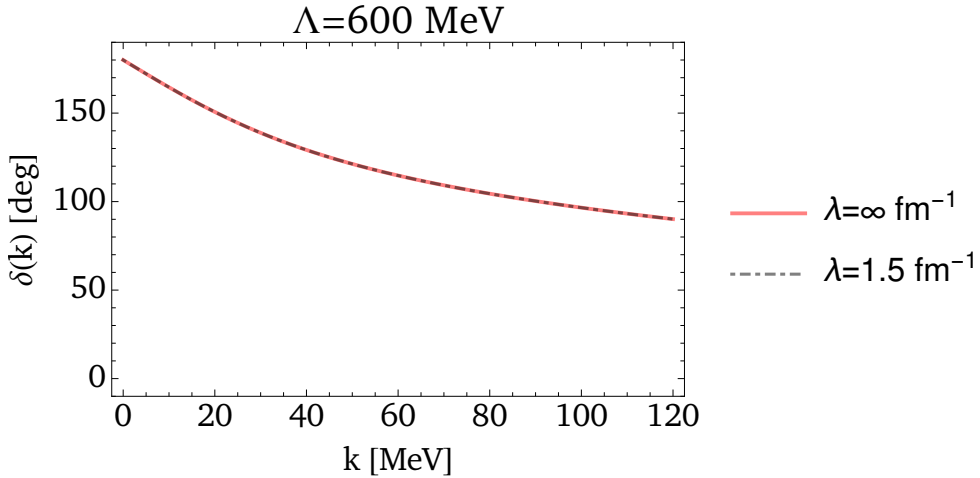


Figure 14: Phase shifts  $\delta(k)$  as a function of the relative momentum  $k$  for two different decoupling scale values  $\lambda = \infty \text{ fm}^{-1}$  and  $\lambda = 1.5 \text{ fm}^{-1}$ . The phase shifts are independent of  $\lambda$ , which shows that observables remain unchanged in the SRG evolution. Since we have a bound state in our  ${}^3S_1$  channel, the phase shift starts at  $180^\circ$  due to Levinson's theorem.

### 3.2 Calculating the U-matrices

The base of every SRG evolution are the transformation matrices  $U_\lambda(k, k')$  since they generate the evolution as shown in Eq. (16) and Eq. (22). The  $U$ -matrices are discontinuous at the diagonal and thus cannot be interpolated. In order to investigate the evolution effects on the longitudinal structure function  $f_L$ , we need a continuous function of  $U_\lambda(k, k')$  as discussed in Sec. 2.6. We therefore split the matrix up into

$$U_\lambda(k, k') = \langle k | k' \rangle + \tilde{U}_\lambda(k, k'), \quad (110)$$

with the identity and a residual matrix  $\tilde{U}(k, k')$ . The matrix elements of  $\tilde{U}_\lambda(k, k')$  for  $\lambda = 1.5 \text{ fm}^{-1}$  are shown Fig. 15. We see that this matrix is indeed smooth and that it is nearly equal to its negative transposed, i.e.  $\tilde{U}_\lambda(k, k') \approx -\tilde{U}_\lambda^T(k, k')$ . The dominating elements are close to the origin, i.e. for small momenta, while for larger momenta the matrix elements go to zero.

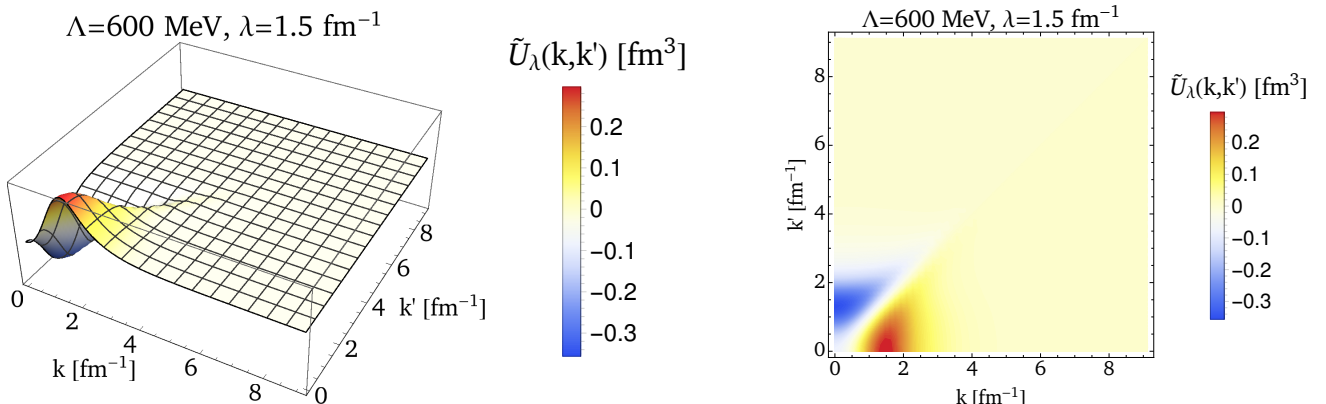


Figure 15: (Left) Surface plot of the matrix elements for  $\tilde{U}_\lambda(k, k') = U_\lambda(k, k') - \langle k | k' \rangle$  at  $\lambda = 1.5 \text{ fm}^{-1}$ . This matrix is continuous and therefore can be interpolated. (Right) Contour plot of  $\tilde{U}_\lambda(k, k')$ .

From the unitarity of the transformation matrix  $U_\lambda$  we can derive an analogous condition for  $\tilde{U}_\lambda$ :

$$\begin{aligned} (\mathbb{1} + \tilde{U}_\lambda)(\mathbb{1} + \tilde{U}_\lambda)^\dagger &= \mathbb{1}, \\ \Rightarrow \mathbb{1} \cdot \tilde{U}_\lambda^\dagger + \mathbb{1} \cdot \mathbb{1} + \tilde{U}_\lambda \tilde{U}_\lambda^\dagger + \tilde{U}_\lambda \cdot \mathbb{1} &= \mathbb{1}, \\ \tilde{U}_\lambda^\dagger + \tilde{U}_\lambda \tilde{U}_\lambda^\dagger + \tilde{U}_\lambda &= 0. \end{aligned} \tag{111}$$

We find that  $\tilde{U}_\lambda$  from Fig. 15 satisfies this condition.

## 4 $f_L$ at different kinematics

We study the longitudinal structure function  $f_L$ , using different kinematics in order to gain further insight on the effects of final-state interactions and the SRG evolution. Since we use pionless EFT, we are restricted to momenta up to roughly the pion mass  $m_\pi = 140$  MeV. Hence, we can only describe the region of outgoing nucleon energies  $E' < 30$  MeV with accuracy, leading to a momentum  $p' \approx 167$  MeV. For photon momenta, we restrict to  $q^2 < 0.7 \text{ fm}^{-2}$ , which leads to  $|\mathbf{q}| \approx 165$  MeV. For momenta far beyond the pion mass, pionless EFT cannot reproduce quantitative results. We nevertheless apply it in this regime to investigate some qualitative behavior.

As already mentioned, the quasi-free kinematics where  $\omega = 0$  is of special interest for us. The relation between final-state energy and photon momentum that defines the quasi-free ridge is given in Ref. [39] as

$$E' = \sqrt{M_D^2 + \mathbf{q}^2} - 2M . \quad (112)$$

When describing the quasi-free ridge in the pionless regime we therefore are limited to  $E' < 5$  MeV due to  $q^2 < 0.7 \text{ fm}^{-2}$ . We look at different kinematics at, close to, and far off the quasi-free ridge in order to study the influence of evolution effects and final-state interactions.

Our results for the longitudinal structure function are scale dependent due to the fact that the potential depends on the cutoff  $\Lambda$ . Making an appropriate choice for the cutoff is our first step. In principle, we can choose whatever  $\Lambda$  we want. This is because our theory is renormalizable. However, the size of  $\Lambda$  is a dominating factor concerning computational requirements. Thus, the cutoff should be chosen as small as possible. The goal is to pick  $\Lambda$  such that the cutoff dependence of our results is below 5%.

In Fig. 16 we plot  $f_L$  as a function of  $\Lambda$  at  $q^2 = 0.5 \text{ fm}^{-2}$  and  $\theta' = 15^\circ$  at the quasi-free ridge. For  $\Lambda > 600$  MeV the influence of the cutoff on  $f_L$  is below 3% in the impulse approximation and below 5% with final-state interactions. Since this satisfies our requirements from above, we conclude that  $\Lambda = 600$  MeV is an appropriate choice.

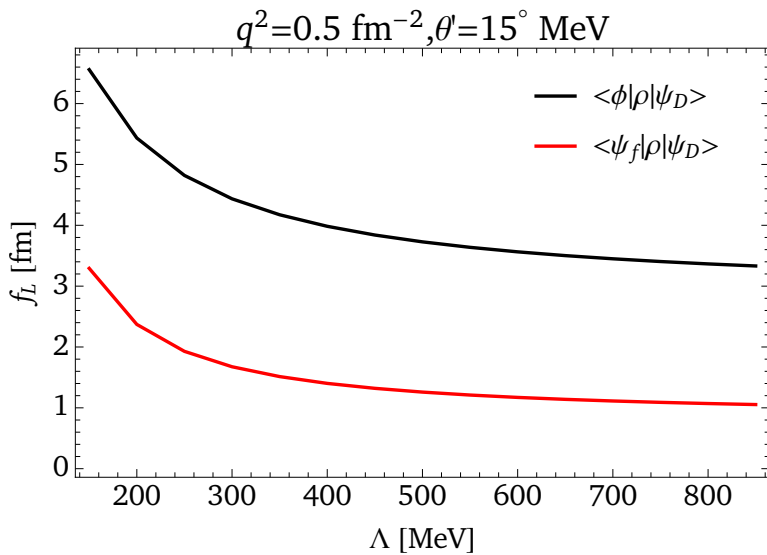


Figure 16: The longitudinal structure function at the quasi-free ridge at  $q^2 = 0.5 \text{ fm}^{-2}$  and  $\theta' = 15^\circ$  as a function of the cutoff  $\Lambda$ . We find that for  $\Lambda > 600$  MeV the result satisfies our requirements for the cutoff.

## 4.1 The quasi-free ridge beyond pionless EFT

As mentioned in the previous section we apply pionless EFT in the regime where it is actually not applicable in order to investigate the quasi-free ridge. Comparing our results to the results of More et al. [3] could give rise to the applicability of pionless EFT in order to make qualitative predictions.

### 4.1.1 Final-state interactions

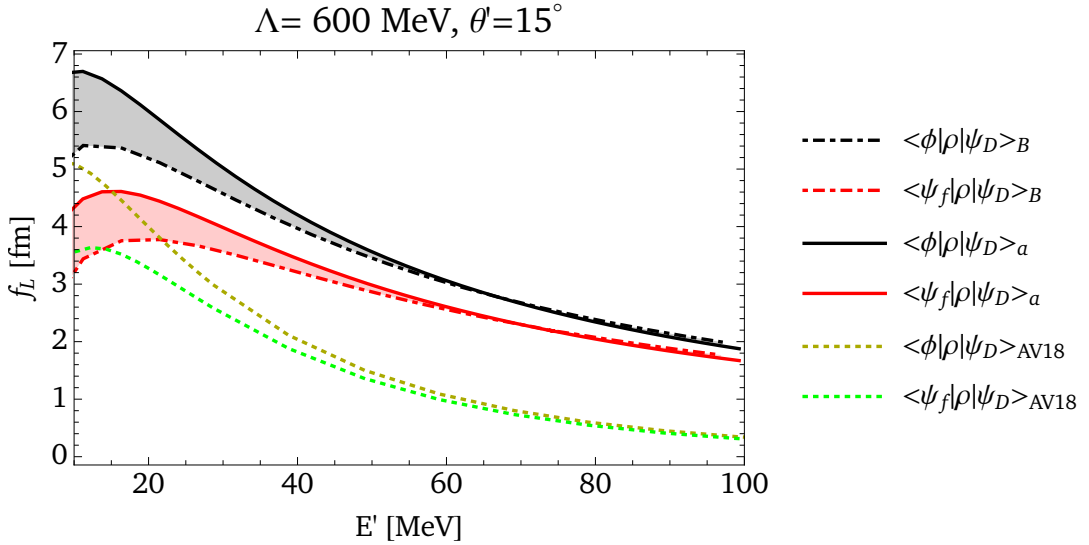


Figure 17: The longitudinal structure function at the quasi-free ridge as a function of outgoing nucleon energy  $E'$  at an angle of  $\theta' = 15^\circ$ . The solid and dotdashed lines refer to the fitting procedure to binding energy and scattering length, respectively, in pionless EFT, while the dotted lines are calculated using the Argonne  $v_{18}$  potential.

We start our investigation with final-state interactions in the high-energy regime. It has been found by More et al. [3] that for some particular kinematical compositions final-state interactions do not contribute. This is called the quasi-free ridge and it is given by Eq. 112. However, this is only the case for sufficiently large values of  $E'$  as shown in Fig 17. Here, we plot the longitudinal structure function  $f_L$  as a function of outgoing nucleon energy  $E'$  at the quasi-free kinematics at an angle of  $\theta' = 15^\circ$ . The results of Ref. [3] are included here and labeled as  $\langle \phi | \rho | \psi_D \rangle_{\text{AV18}}$  and  $\langle \psi_f | \rho | \psi_D \rangle_{\text{AV18}}$  for impulse approximation and included final-state interactions, respectively. Our result has several qualitative characteristics in common with the Argonne  $v_{18}$  calculation. In both calculations the longitudinal structure function decreases for larger  $E'$ . In addition to that, for the Argonne  $v_{18}$  potential as well as in pionless EFT final-state interactions become negligible when the outgoing nucleons have a larger energy. Furthermore, including final-state interactions in the low-energy area in both cases leads to a suppressed longitudinal structure function. However, there are also differences. The Argonne  $v_{18}$  calculation leads to a smaller  $f_L$  over the whole range of energies and the impact of final-state interactions becomes smaller than 5% at  $E' \approx 50$  MeV. In contrast to that, in pionless EFT this happens only for  $E' > 100$  MeV. Nevertheless, we conclude that pionless EFT is suited to at least qualitatively describe physics beyond its breakdown scale  $\Lambda_b \approx m_\pi$ . This observation is also confirmed by Fig. 18. Here, we plot the ratio  $|f_L^{\text{IA}} - f_L^{\text{FSI}}| / f_L^{\text{IA}}$ , where the superscript "IA" refers to impulse approximation, while "FSI" refers to impulse approximation and included final-state interactions. This means that a small ratio is equivalent to final-state interactions contributing weakly to  $f_L$ . Using pionless EFT, we are still able to reproduce the essence of Fig. 11, even though we apply this theory far beyond the pionless regime. Along and close to the quasi-free ridge, the relative strength of final-state interactions becomes smaller than 15% for  $q^2 > 4 \text{ fm}^{-2}$ . Far off the quasi-

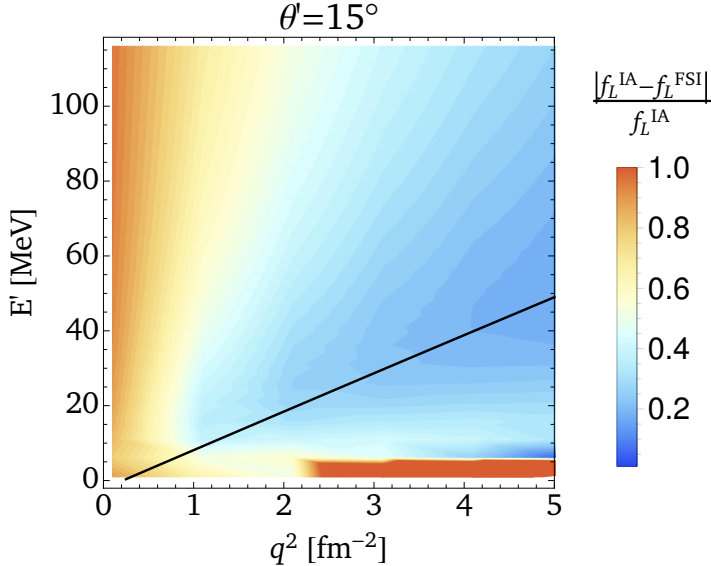


Figure 18: The relative strength of final state interactions for momenta beyond pionless EFT. In agreement with Fig. 11 final-state interactions become small at the quasi-free ridge (black solid line) beyond the pionless regime and large far off the same. The superscripts "IA" and "FSI" refer to impulse approximation and included final-state interactions, respectively.

free ridge, final-state interactions become very large especially for small energies  $E'$  and large photon momenta  $q^2$ . Note that the ratio in this area is way larger than 1.

In the calculations for  $\langle \phi | \rho | \psi_D \rangle_B$  and  $\langle \psi | \rho | \psi_D \rangle_B$  of Fig. 17, we fit  $C_0$  to the deuteron binding energy  $E_B = -2.225$  MeV. Another possibility is to fit  $C_0$  to the scattering length of the  ${}^3S_1$  channel  $a_T = 5.4$  fm $^{-1}$ . Comparing both possibilities, we find that the fitting method of  $C_0$  has a rather large influence on  $f_L$  of about 30% for small energies. As we go to larger energies, we find that both possibilities converge to the same value. This result agrees perfectly with the expectations for pionless EFT. Our uncertainties are then given by the two different possibilities of fitting  $C_0$ , leading to the uncertainty bands shown in Fig. 17. The results for the Argonne  $v_{18}$  potential fall outside our bands, in agreement with the limited quantitative applicability of pionless EFT. In the low-momentum regime however, the Argonne  $v_{18}$  calculation should fall inside our uncertainty bands. We will indeed find this, as shown in Sec. 4.3.

#### 4.1.2 Evolution effects

The next step is to investigate evolution effects, both in the impulse approximation and with included final-state interactions. As in the previous section on the SRG results, we use a value of  $\lambda = 1.5$  fm $^{-1}$  for the decoupling scale. Figure 19 shows the longitudinal structure function  $f_L$  at the quasi-free ridge at an angle of  $\theta' = 15^\circ$  for our pionless calculation (left) and for the Argonne  $v_{18}$  potential (right). In the latter calculation evolution effects are very small just like final-state interactions. In contrast to that, in pionless EFT evolution effects become more important for larger energies. This will be discussed in more detail below.

One central observation is that the fully evolved matrix elements, which means that current operator as well as initial and final-state wave function are evolved, lead perfectly to the same  $f_L$  as the un-evolved matrix elements. This confirms that observables remain invariant in the SRG evolution and is an important check for the correctness of our calculation. Even though we can only describe the region  $E' < 5$  MeV in pionless EFT, the unitarity of the SRG is independent of this fact. That means we can also study qualitatively the evolution effects for  $E' > 5$  MeV.

We first investigate the impulse approximation. For small energies evolution effects are tiny, even though it has a small effect if current operator and deuteron wave function are both evolved, whereas

the evolution of the current operator alone has a negligible effect. This is shown in the upper left panel of Fig. 20, where we plot  $f_L$  as a function of  $\theta'$  in the region of  $20^\circ \leq \theta' \leq 30^\circ$ . When going to larger energies  $E'$ , this changes, meaning that evolution effects become more important. We know from the unitarity of the SRG that

$$\langle \phi | \rho | \psi_D \rangle = \langle \phi^\lambda | \rho^\lambda | \psi_D^\lambda \rangle, \quad \langle \psi | \rho | \psi_D \rangle = \langle \psi^\lambda | \rho^\lambda | \psi_D^\lambda \rangle, \quad (113)$$

is satisfied. This allows an interpretation of our results in which the evolution of the deuteron wave function plays a crucial role. We first look at the behavior of  $\langle \phi^\lambda | \rho^\lambda | \psi_D \rangle$ . Comparing this matrix element with the fully-evolved matrix element, the only difference is the evolution of the deuteron wave function. In the low-energy region for  $q^2 = 1 \text{ fm}^{-2}$ , the argument

$$y = \sqrt{p'^2 - p'q \cos \theta' + \frac{q^2}{4}} \quad (114)$$

of the latter (see Sec. 2.4) is a maximum of  $y = 1 \text{ fm}^{-1}$  for  $\theta' = 180^\circ$ . Thus, the deuteron wave function is, except for the integrals which are independent of kinematics, mainly probed in the low-momentum region. As shown in Fig. 13, in this region there is only a small difference between evolved and unevolved wave function and therefore evolution effects are small. As we go to larger  $q^2$  the argument  $y$  also becomes larger. The deuteron wave function is then probed at momenta where evolution effects contribute, leading to increased effects on the longitudinal structure function. For the calculation using the  $\langle \phi | \rho^\lambda | \psi_D \rangle$  matrix element, we observe something similar. This matrix element is the full  $B$ -term from Eq. 59 with the unevolved deuteron wave function, which means that we have the impulse approximation extended by the unevolved  $B_1$ ,  $B_2$ , and  $B_3$  terms (eqs. (71), (72) and (78)) that are the result of splitting up the transformation matrix. In the left panel of Fig. 21 we show the strength of these three terms for evolved and unevolved deuteron wave function. For small energies these different terms

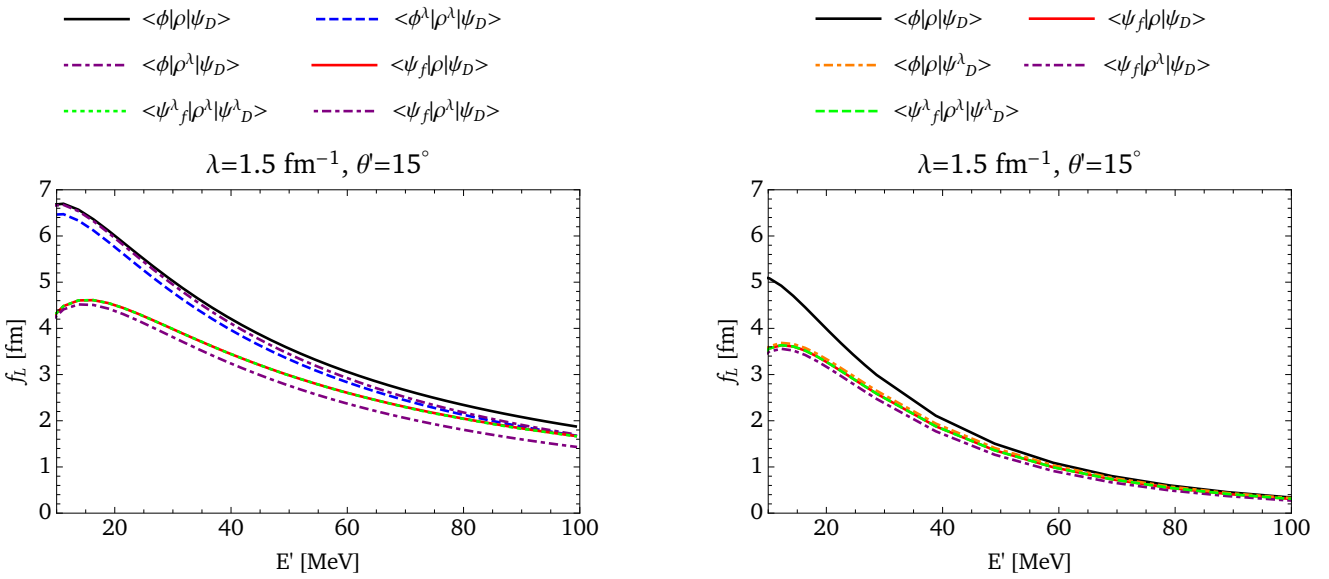


Figure 19: (Left) The longitudinal structure function at the quasi-free ridge as a function of outgoing nucleon energy  $E'$  at an angle of  $\theta' = 15^\circ$ . The fully-evolved matrix elements fit perfectly to the unevolved ones, which confirms the unitarity of the transformation matrices. The partly-evolved matrix elements however differ from the unevolved calculation as we go to larger energies. (Right) The same calculation obtained by More et al. [3] for the Argonne  $v_{18}$  potential.

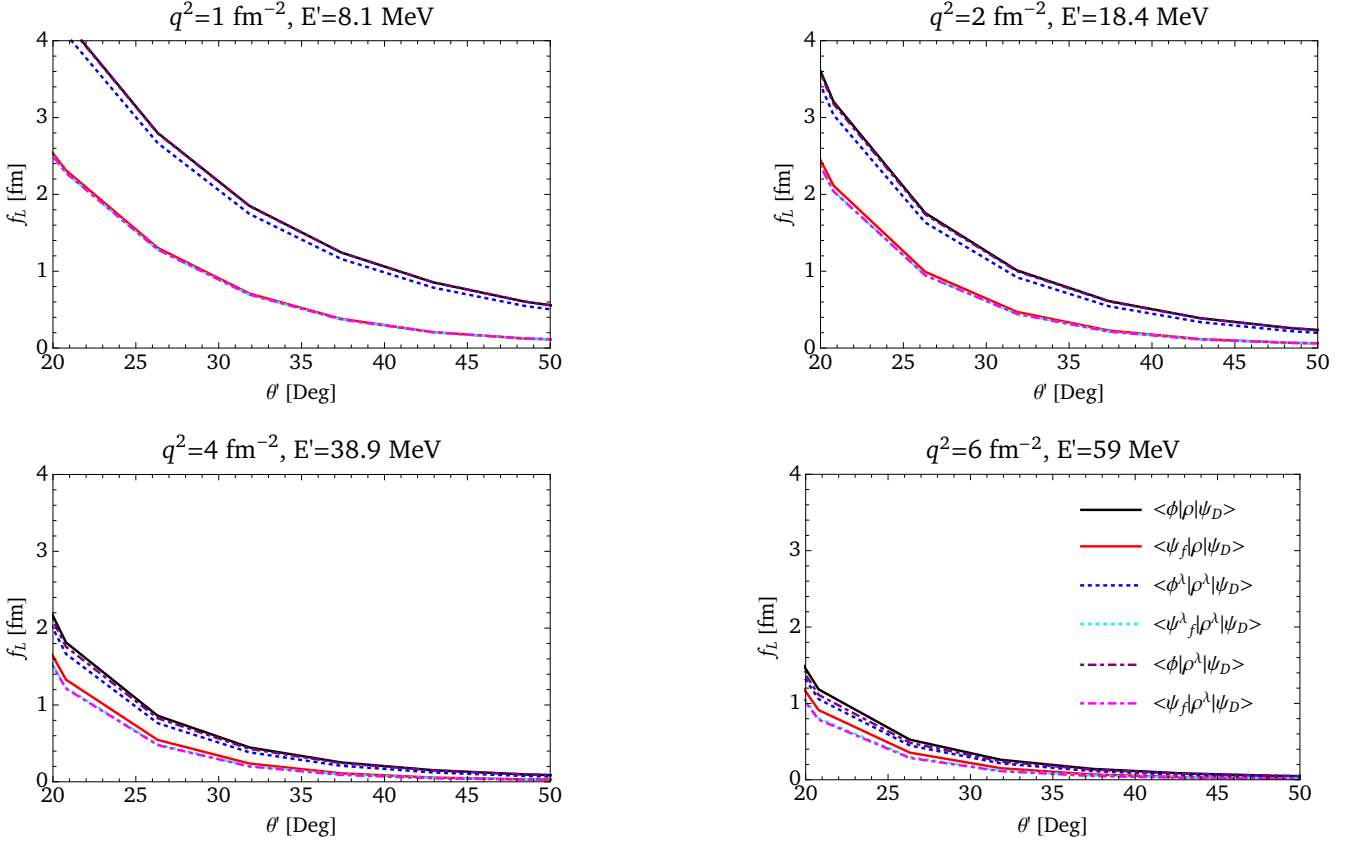


Figure 20: Kinematic dependence on the SRG evolution effects at the quasi-free ridge as a function of  $\theta'$ . As we go to larger  $E'$ , the influence of the partly-evolved matrix elements shift.

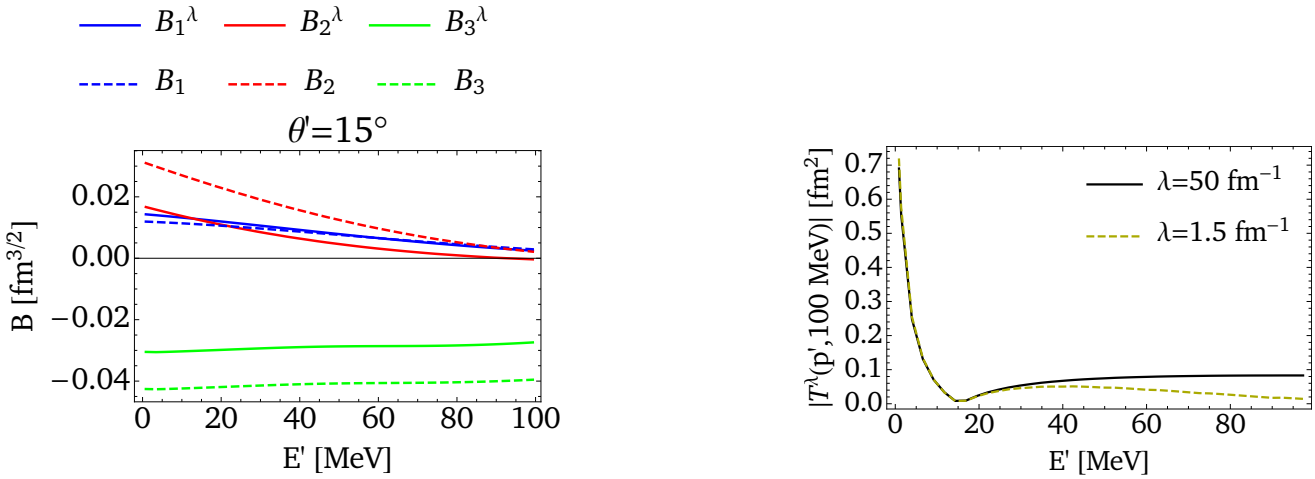


Figure 21: (Left) Strength of the different evolution terms for the unevolved deuteron wave function ( $B_1$ - $B_3$ ) and for the evolved deuteron wave function ( $B_1^\lambda$ - $B_3^\lambda$ ). (Right) Absolute value of the half on-shell  $T$ -matrix  $T^\lambda(p', 100 \text{ MeV})$  for  $\lambda = 50 \text{ fm}^{-1}$  and  $\lambda = 1.5 \text{ fm}^{-1}$ . The momentum  $p'$  is given by  $E' = p'^2/M$ .

nearly cancel each other. For larger energies the strength of  $B_1$  and  $B_2$  become smaller, whereas  $B_3$  is nearly independent of kinematics. Thus, the impact of evolution effects on  $f_L$  becomes larger as we go to higher energies.

The same observations hold for the final-state interactions, but the effects are smaller in this case. This is due to the  $T$ -matrix that mainly determines the final-state interactions. The absolute value of the half

on-shell  $T$ -matrix  $T(p', k = 100 \text{ MeV})$  and  $T^\lambda(p', k = 100 \text{ MeV})$  as a function of  $E'$  is shown in the right panel of Fig. 21. We find that the SRG affects the  $T$ -matrix mainly for  $E' > 30 \text{ MeV}$ . This is also the region where the evolved final-state interactions begin to differ from the unevolved result. Hence, especially for  $E' < 30 \text{ MeV}$  the relative strength of evolution effects is smaller. Note that the value  $k = 100 \text{ MeV}$  considered here is arbitrary but representative.

## 4.2 Evolution effects in the pionless regime

In Sec. 4.1.2 we investigated evolution effects at the quasi-free ridge outside the range of validity of pionless EFT. We now focus on energies we can describe within our theory and compare results at the quasi-free ridge with results at different kinematics in order to understand the special features of the quasi-free ridge.

### 4.2.1 At the the quasi-free ridge

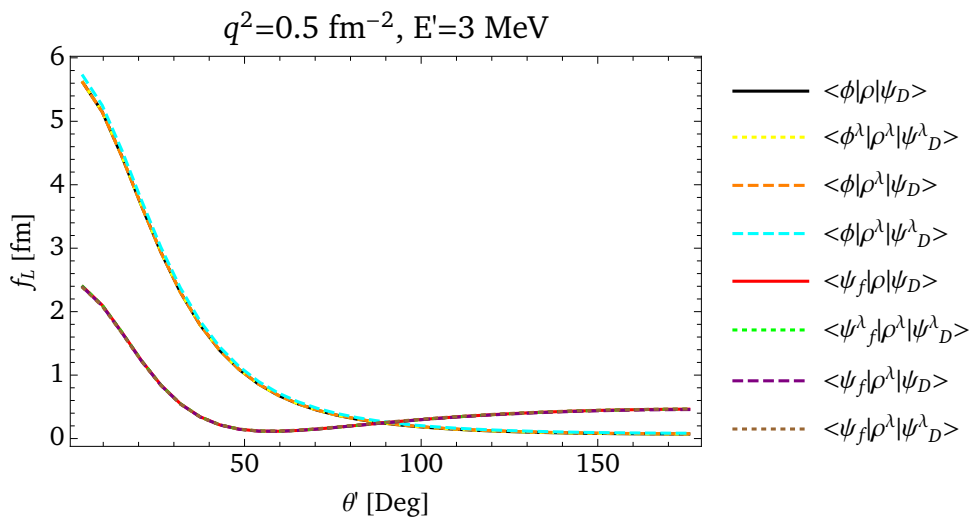


Figure 22: The longitudinal structure function at the quasi-free ridge for  $q^2 = 0.5 \text{ fm}^{-2}$  and  $E' = 3.0 \text{ MeV}$  as a function of  $\theta'$ . The influence of evolution effects is tiny in the impulse approximation and negligible with final-state interactions for these kinematics.

We start with the quasi-free kinematics. In Fig. 22 we show the longitudinal structure function as a function of the angle  $\theta'$  for  $q^2 = 0.5 \text{ fm}^{-2}$  and  $E' = 3.0 \text{ MeV}$ . Similarly to the upper left result of Fig. 20 we find that evolution effects are very small for the impulse approximation and negligible if final-state interactions are included. A detailed explanation for this is given in Sec. 4.1.2. Again we want to emphasize that this observation shows that final-state interactions and evolution effects are not necessarily correlated. For small energies at the quasi-free ridge, evolution effects are almost negligible, while final-state interactions are large. As shown by More et al. [3], in the high-momentum area there is a correlation. Investigating this different behavior would be interesting in future work.

### 4.2.2 Close to the quasi-free ridge

Moving away from the quasi-free ridge we would expect that evolution effects become slightly more important compared to the quasi-free kinematics from above. In Fig. 23 we plot  $f_L$  as a function of  $\theta'$  for  $q^2 = 0.5 \text{ fm}^{-2}$  and  $E' = 10 \text{ MeV}$ . Compared to Fig. 22, we find that the longitudinal structure function becomes larger for both impulse approximation and with included final-state interactions. The influence of evolution effects however is still very small in the impulse approximation and negligible with final-state interactions. Even though we would have expected small changes, this result is still in

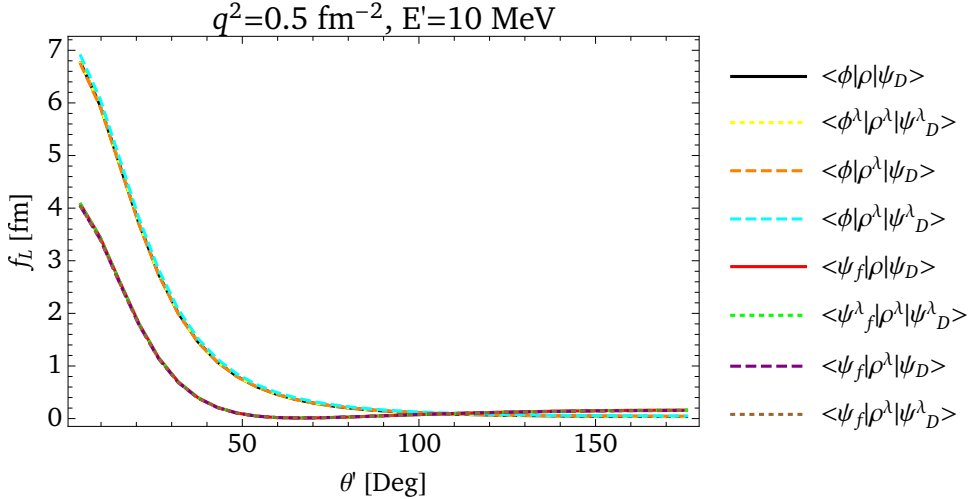


Figure 23: The longitudinal structure function at the quasi-free ridge for  $q^2 = 0.5 \text{ fm}^{-2}$  and  $E' = 10 \text{ MeV}$  as a function of  $\theta'$ . The influence of evolution effects are still tiny for these kinematics, even though we are not at quasi-free kinematics anymore.

agreement with Fig. 11. For the kinematics we use, we are only off the quasi-free ridge with respect to the pionless regime. On a larger scale as in Fig. 11, our particular kinematic used here is still very close to the quasi-free ridge. However, our observation raises the question if there is a potential dependence in the relative strength of evolution effects. Investigating the low-energy region with the Argonne  $v_{18}$  potential could give rise to this question.

#### 4.2.3 Far off the quasi-free ridge

Regarding the results of the previous section, we now investigate whether evolution effects can become relevant in the pionless regime. In order to investigate this, we choose  $q^2 = 0.1 \text{ fm}^{-2}$  and  $E' = 30 \text{ MeV}$ . This kinematics is as far off the quasi-free ridge as possible within the pionless regime. We calculate  $f_L$  as a function of  $\theta'$  as shown in Fig. 24. In the impulse approximation we find that evolution effects

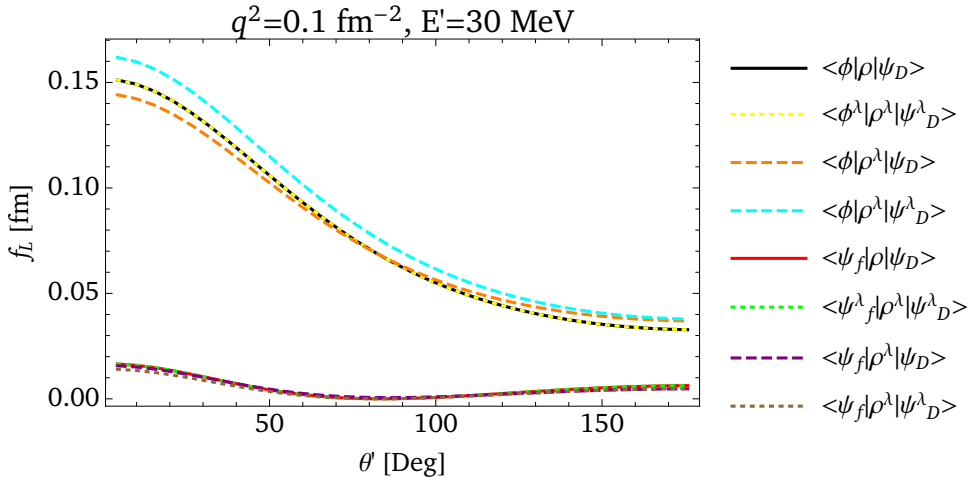


Figure 24: The longitudinal structure function at the quasi-free ridge for  $q^2 = 0.1 \text{ fm}^{-2}$  and  $E' = 30 \text{ MeV}$  as a function of  $\theta'$ . The influence of evolution effects are not negligible anymore in the impulse approximation for this paricular kinematics. When final-state interactions are included, evolution effects are small.

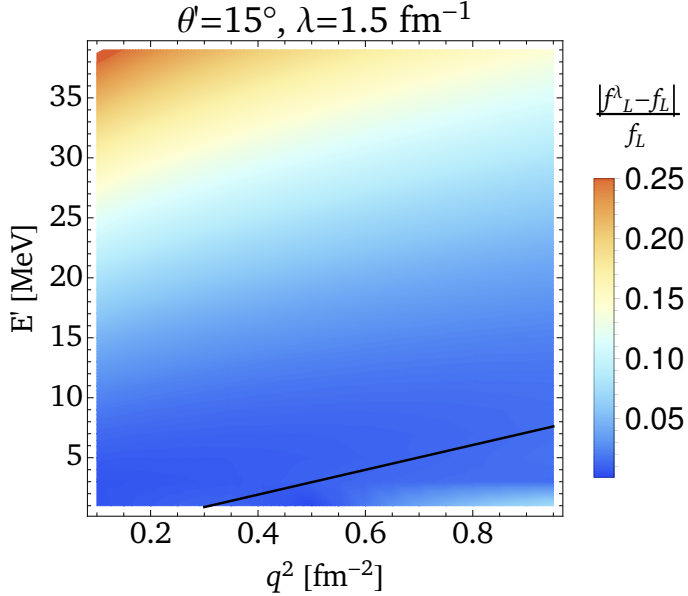


Figure 25: The relative influence of the effects coming from the evolution of the one-body current. These effects are, in agreement with our expectation, small around the quasi-free ridge (black solid line) and large far off. For both  $f_L^\lambda$  and  $f_L$  final-state interactions are included.

have a non-negligible influence. Especially in the case of evolved current operator and deuteron wave function we have a deviation of roughly 7% from the unevolved result. When final-state interactions are included, we observe some similar effects. The relative strength of evolution effects increases to roughly 20%. Our results lead to the conclusion that within pionless EFT evolution effects can become important for kinematics far off the quasi-free ridge.

In Fig. 25 we plot the ratio  $|f_L^\lambda - f_L|/f_L$  for an angle of  $\theta' = 15^\circ$ . For  $f_L^\lambda$  the one-body current is evolved, such that the underlying matrix element is  $\langle \psi_f | \rho^\lambda(\mathbf{q}) | \psi_D \rangle$ , while for  $f_L$  we use the unevolved matrix element  $\langle \psi_f | \rho(\mathbf{q}) | \psi_D \rangle$ . In agreement with our expectations from Fig. 11 and our previous results we find that these effects are very small around the quasi-free ridge (black solid line), while they become large for kinematics far off the latter. However, we want to emphasize here that we are looking here at kinematics well beyond the pionless regime. In a more strict limitation of momenta, allowing  $E' < 20$  MeV and  $q^2 < 0.5$  fm $^{-2}$ , evolution effects are always below 10%. Hence, our results lead to the conclusion that induced two-body currents do not contribute strongly to observables in the pionless regime.

#### 4.2.4 Evolution effects for different binding energies

We already know that evolution effects depend on kinematics. Another interesting question is whether evolution effects depend on the strength of the potential. One way to investigate this is keeping the cutoff fixed and varying the binding energy of the deuteron. A stronger binding then corresponds to a more attractive potential. In the left panel of Fig. 26 we plot the longitudinal structure function  $f_L$  as a function of  $\theta'$  for  $q^2 = 0.1$  fm $^{-2}$  and  $E' = 30$  MeV. The solid lines are calculated via the unevolved matrix element  $\langle \psi_f | \rho(\mathbf{q}) | \psi_D \rangle$ , while the dotted lines have the one-body current evolved, i.e., the matrix element is  $\langle \psi_f | \rho^\lambda(\mathbf{q}) | \psi_D \rangle$ . Note that in all the calculations in this section final-state interactions are included.

Plotting the relative influence of evolution effects, which is shown in the right panel of Fig. 26, we find that evolution effects become more important for a stronger binding energy and therefore directly depend on the strength of the potential. Furthermore, this effect is independent of kinematics. In Fig. 27 we show the influence of evolution effects for the other extreme of kinematics, i.e.,  $q^2 = 0.7$  fm $^{-2}$

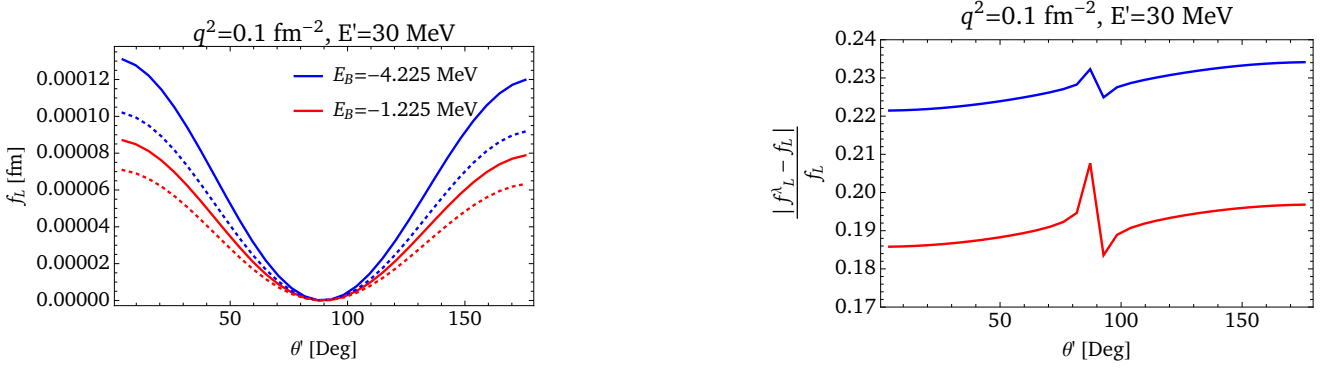


Figure 26: (Left) The longitudinal structure function  $f_L$  as a function of  $\theta'$  for  $q^2 = 0.1 \text{ fm}^{-2}$  and  $E' = 30 \text{ MeV}$  for two different binding energies  $E_B = -1.225 \text{ MeV}$  and  $E_B = -4.225 \text{ MeV}$ . For this particular kinematics the nucleons have the largest momenta valid in pionless EFT, while the photon momentum is very small. The solid lines refer to the unevolved matrix element, while the dotted lines are calculated with the evolved operator, i.e.,  $\langle \psi_f | \rho^\lambda | \psi_D \rangle$ . (Right) The relative influence of evolution effects for the evolved one-body current on  $f_L$ . The peak at  $\theta' \approx 90^\circ$  is due to numerical artifacts. The superscript "λ" refers to the evolved one-body current.

and  $E' = 0.01 \text{ MeV}$ , which corresponds to large photon momentum and small nucleon momentum. Nevertheless, we observe the same behavior for the relative influence of evolution effects, meaning that they become larger for stronger binding. This observation also holds at the quasi-free ridge as shown in Fig. 28. The fact that the relative strength of evolution effects on  $f_L$  is peaked in Figs. 26 and 28 is due to numerical artifacts.

Our observation is not trivial. The behavior of  $f_L$  itself with changing binding energy depends on kinematics. While in Fig. 27 and Fig. 28 the longitudinal structure function becomes smaller for stronger binding, in Fig. 26 we observe the opposite behavior. From this observation it is obvious that the strength of the potential does not proportionally affect all the other quantities. However, we find that the strength of evolution effects does depend proportionally on the potential. The reason is that the transformation matrices correlate with the potential. The influence of  $E_B$  on  $\tilde{U}$  is shown in Fig. 29, where we plot the latter for  $E_B = -1.225 \text{ MeV}$  (left panel) and  $E_B = -4.225 \text{ MeV}$  (right panel). We find that  $\tilde{U}$  becomes

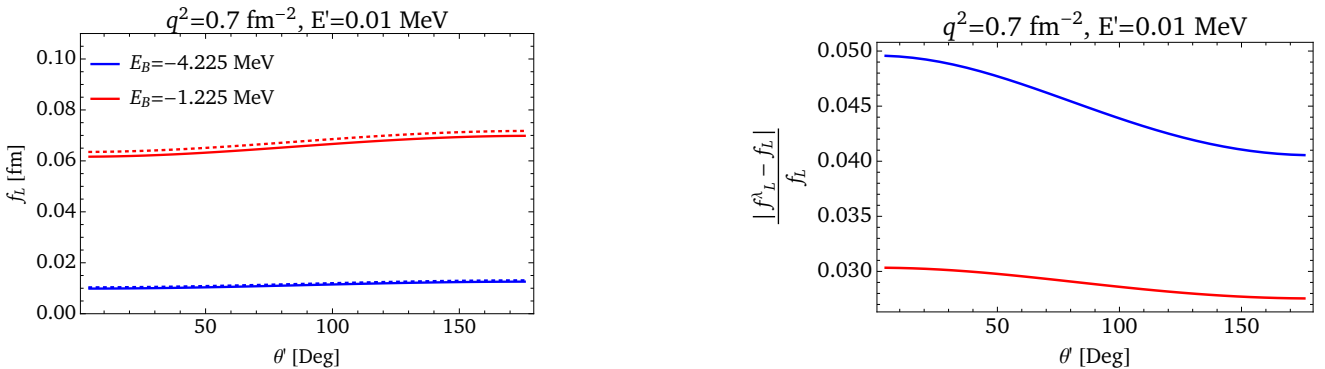


Figure 27: (Left) The longitudinal structure function  $f_L$  as a function of  $\theta'$  for  $q^2 = 0.7 \text{ fm}^{-2}$  and  $E' = 0.01 \text{ MeV}$  for two different binding energies  $E_B = -1.225 \text{ MeV}$  and  $E_B = -4.225 \text{ MeV}$ . For this particular kinematics the nucleons have the smallest momenta valid in pionless EFT, while the photon momentum is very large. The solid lines refer to the unevolved matrix element, while the dotted lines are calculated with the evolved operator, i.e.,  $\langle \psi_f | \rho^\lambda | \psi_D \rangle$ . (Right) The relative influence of evolution effects for the evolved one-body current on  $f_L$ . The superscript "λ" refers to the evolved one-body current.

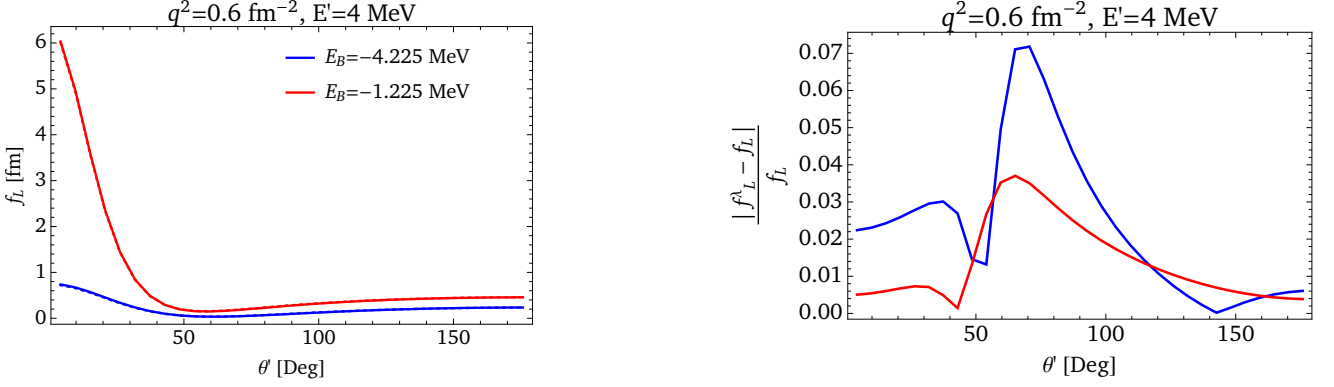


Figure 28: (Left) The longitudinal structure function  $f_L$  as a function of  $\theta'$  for  $q^2 = 0.6 \text{ fm}^{-2}$  and  $E' = 4 \text{ MeV}$  for different binding energies. This kinematics is at the quasi-free ridge. (Right) The relative influence of evolution effects for the evolved one-body current on  $f_L$ . Since we are at the quasi-free ridge evolution effects are very small. The peak at  $\theta' \approx 70^\circ$  is due to numerical artifacts. The superscript " $\lambda$ " refers to the evolved one-body current.

larger for stronger binding especially in the low-momentum area. This necessarily leads to increased evolution effects.

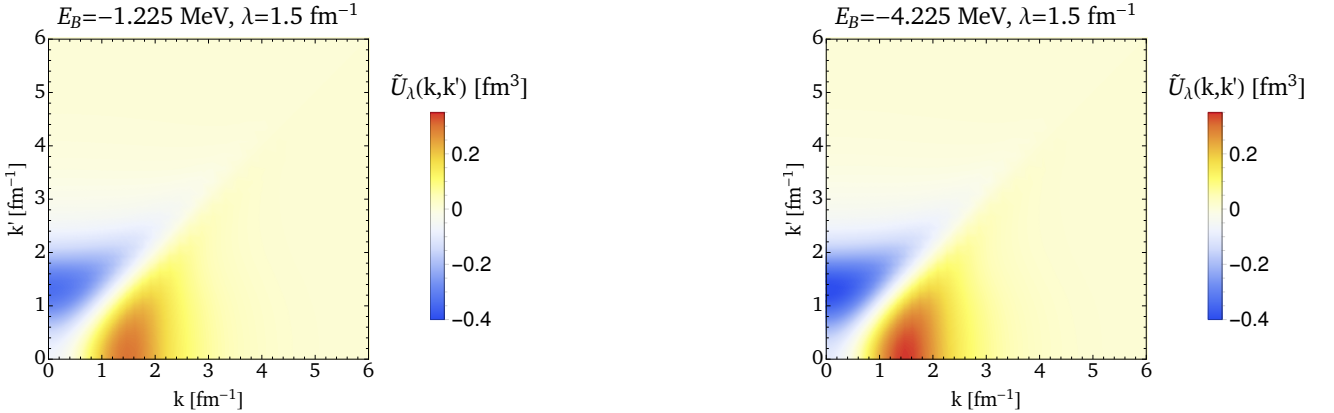


Figure 29: The smooth part of the transformation matrix  $\tilde{U}(k, k')$  for (left)  $E_B = -1.225 \text{ MeV}$  and (right)  $E_B = -4.225 \text{ MeV}$ . The matrix elements become larger for stronger binding because of the direct dependence to the potential.

### 4.3 Final-state interactions in the pionless regime

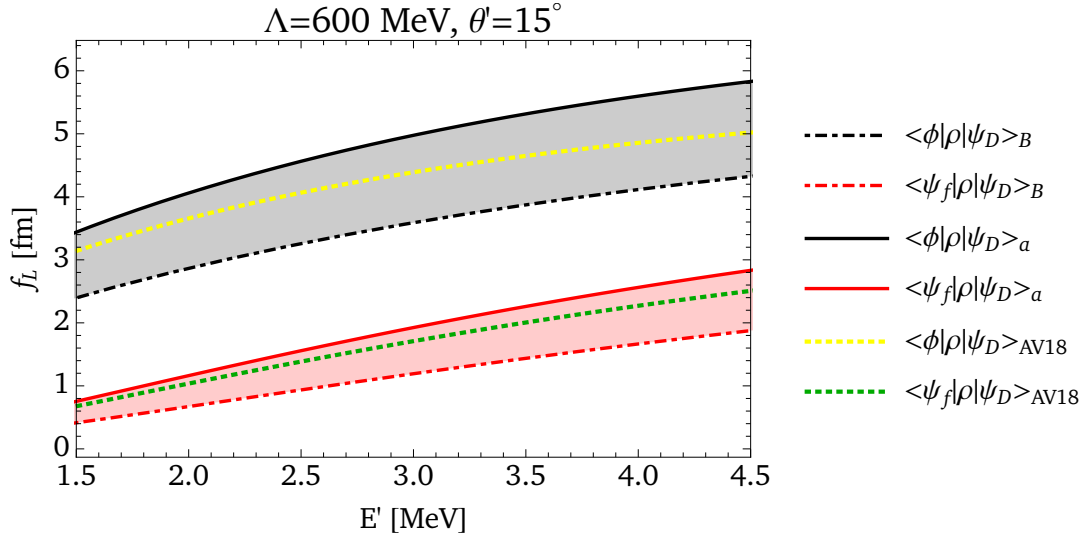


Figure 30: The longitudinal structure function at the quasi-free ridge as a function of outgoing nucleon energy  $E'$  at an angle of  $\theta' = 15^\circ$ . We find that the Argonne  $v_{18}$  calculation lies within the uncertainty band of our pionless calculation.

Since we now have investigated the evolution effects within and beyond pionless EFT, we come to the second big goal of this work, which is understanding final-state interactions at the quasi-free ridge. In Fig. 30 we show  $f_L$  as a function of  $E'$  at the quasi-free ridge for small energies. The uncertainties are quantified in the same manner as in Fig. 17, i.e., by fitting  $C_0$  to the deuteron binding energy and the scattering length. The related matrix elements in the impulse approximation are  $\langle \phi | \rho | \psi_D \rangle_B$  and  $\langle \phi | \rho | \psi_D \rangle_a$ , respectively, and analogously for included final-state interactions. Our plot shows exactly what we expected for pionless EFT. The result using the Argonne  $v_{18}$  potential falls perfectly within the uncertainty bands, both in the impulse approximation and with final-state interactions. Especially in the latter case, the agreement to the result we obtain when  $C_0$  is fitted to  $a_T$  is a maximum of 10% for  $E' = 4.5$  MeV. Our result confirms that pionless EFT is indeed very well suited to describe deuteron electrodisintegration in the low-energy region, as already found by Christlmeier and Grießhammer [7]. Furthermore, the agreement with More et al. [3] is very promising considering further investigations.

Figure 30 also confirms what we expected from Fig. 17: final-state interactions are very important in the low-energy region also at the quasi-free ridge. Hence, the quasi-free ridge is not quasi-free in this regime! Our hypothesis is that this is due to the  $T$ -matrix becoming large for small nucleon momenta  $p'$  in order to reproduce the large scattering length. We can test this hypothesis by varying the binding energy since a weak binding corresponds to a large scattering length and vice versa. In the case of weak binding, the  $T$ -matrix should be the dominating quantity leading to strong final-state interactions.

#### 4.3.1 Variation of the binding energy

As mentioned in the previous section, our goal is to vary the binding energy in order to investigate the influence of final-state interactions at the quasi-free ridge for small momenta. The significant advantage of pionless EFT is that we can choose whatever binding energy we want and adjust  $C_0$  to the value. Using phenomenological potentials like the Argonne  $v_{18}$  potential, such a variation would not be readily possible.

When varying the binding energy, we expect the following behavior for final-state interactions: a weak binding energy corresponds to a large scattering length. The scattering length is directly connected to the on-shell  $T$ -matrix via

$$a_s = 2\mu \lim_{p' \rightarrow 0} \text{Re}[T(p', p')]. \quad (115)$$

Because of the fact that the  $T$ -matrix is continuous, we expect that the on-shell element also determines the behavior of the whole half on-shell  $T$ -matrix. The latter is a dominating ingredient contributing to final-state interactions. Hence, we expect that final-state interactions become relatively more important for kinematics such that  $p'$  is small at weak binding. For strong binding, we expect the opposite behavior: the scattering length becomes small in this case and with it the  $T$ -matrix, resulting in relatively weak final-state interactions. Note that a "small" scattering length is still large compared to the range of pion exchange  $r = 1.4 \text{ fm}^{-1}$ . For a binding energy  $E_B = -4.225 \text{ MeV}$  we have, for example,  $a_T = 3.67 \text{ fm}^{-1}$ . Otherwise, the nonperturbative resummation of pionless EFT would not work.

The half on-shell  $T$ -matrix  $T(p', k)$  as a function of the momentum  $k$  is shown in the left panel of Fig. 31 for different binding energies  $E_B$  at  $q^2 = 0.25 \text{ fm}^{-2}$  and  $p' = 18.6 \text{ MeV}$ . In agreement with our expectations, we indeed find that the  $T$ -matrix becomes large for weaker binding of the deuteron in the whole range of momenta. This dependence is very strong for small momenta  $k$  (close to  $p'$  in order to reproduce the scattering length) and weak in the high-momentum area.

In the left panel of Fig. 32 we plot the longitudinal structure function  $f_L$  for  $q^2 = 0.25 \text{ fm}^{-2}$ ,  $p' = 18.6 \text{ MeV}$ , and  $\theta' = 15^\circ$  in the impulse approximation and with final-state interactions. Note that this kinematics is only at the quasi-free ridge for  $E_B = -2.225 \text{ MeV}$  due to the deuteron mass  $M_D = 2M + E_B$  (see Eq. (112)). In the latter case  $f_L$  is very close to zero, meaning that the contribution of final-state interactions is nearly as large as the impulse approximation. This is also shown in the right panel of Fig. 32 where we plot the ratio  $(f_L^{IA} - f_L^{FSI})/f_L^{IA}$  as a function of  $E_B$ . The superscripts "IA" and "FSI" refer to impulse approximation and included final-state interactions, respectively. For strong binding, final-state interactions are very important, while they become less important as we go to weaker binding. This observation is in contradiction to our naive expectations. Apparently, the  $T$ -matrix is not the dominating part of final-state interactions for these kinematics. Looking at the  $F_4$  terms (see Eq. (86)), we note that, besides the  $T$ -matrix, also the deuteron wave function  $\psi_D$  is important. In the right panel of Fig. 31 we show  $\psi_D(k)$  as a function of momentum  $k$  for different binding energies  $E_B$ . For momenta  $k < 0.25 \text{ fm}^{-1}$ , the effects of  $E_B$  on  $\psi_D(k)$  are huge. For momenta larger than that, the effect of different binding energies becomes negligible. Note that the wave functions nevertheless are normalized

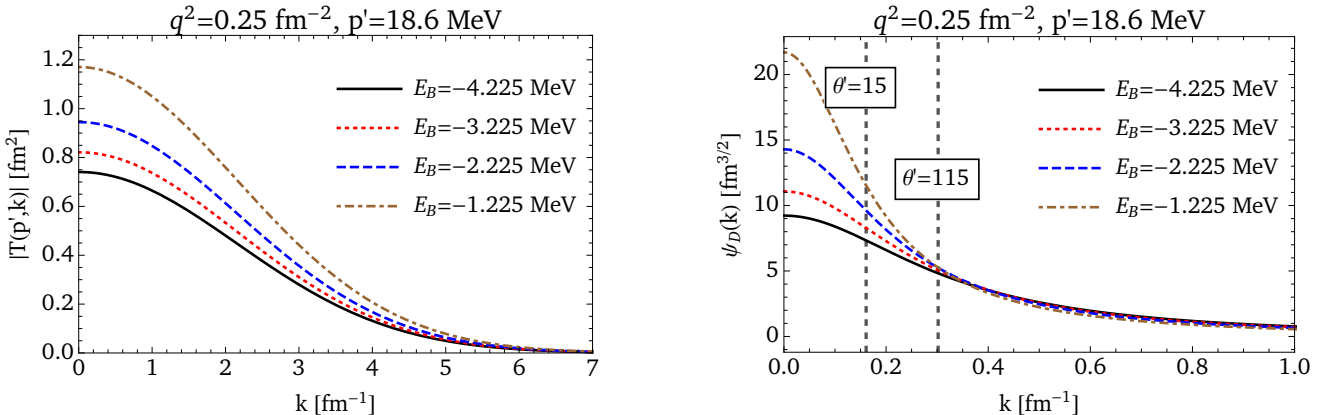


Figure 31: (Left) The deuteron wave function for different value of  $E_B$  in the low-momentum area. (Right) The absolute value of the half on-shell  $T$ -matrix for different binding energies.

to unity. The large changes for low momenta are compensated over the whole range of momenta such that the integral

$$\frac{2}{\pi} \int dp p^2 |\psi_D(p)|^2 = 1 \quad (116)$$

remains invariant.

Using these insights, we now further investigate the results of Fig. 32. To this end, in Fig. 33 we plot (left panel) the on-shell  $T$ -matrix and (right panel) the deuteron wave function for momentum  $k = y$  for the very same kinematics as in Fig. 32. The latter case corresponds to a plot of the wave function along the dashed line for  $\theta' = 15^\circ$  in Fig. 31. In both cases, we observe the expected behavior: the  $T$ -matrix becomes large for weak binding in order to reproduce the increasing scattering length. The wave function  $\psi_D(y)$  also becomes large for weak binding since it is probed at  $y = 0.18 \text{ fm}^{-1}$ , i.e., the area where varying the binding energy has a strong influence. The important question is: which quantity is stronger effected by the binding energy? In order to analyze this, we plot in Fig. 34 the deuteron wave function  $\psi_D(y)$  and the on-shell  $T$ -matrix  $T(p', p')$  as a function of the binding energy normalized to the physical binding energy  $E_B = -2.225 \text{ MeV}$ . For all  $E_B$  the slope of the deuteron wave function is larger than the slope of the  $T$ -matrix. This means that the deuteron wave function is stronger affected by the variation of  $E_B$ . As shown in Eq. (73) the longitudinal structure function in the impulse approximation is basically given by the deuteron wave function  $\psi_D(y)$ . Hence, for weak binding especially the impulse

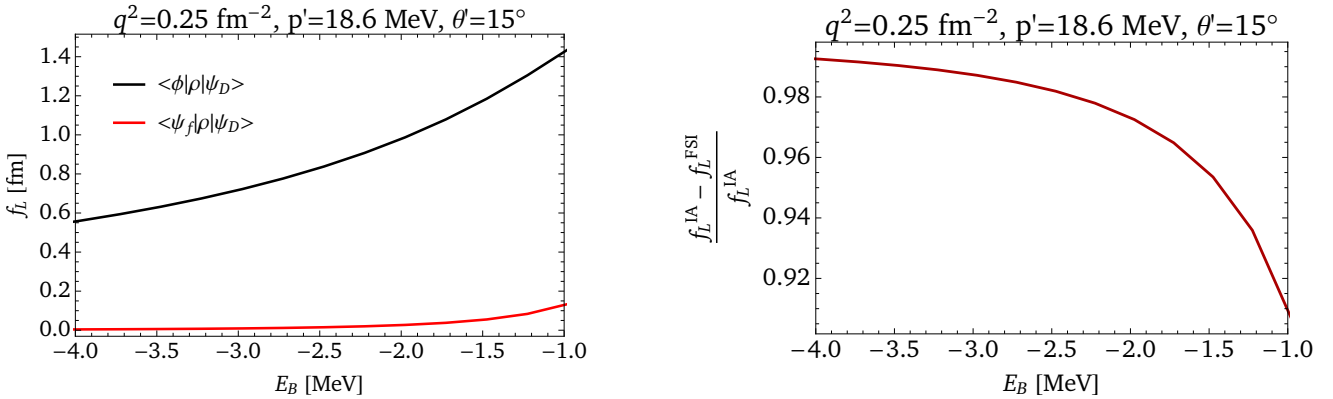


Figure 32: (Left) The longitudinal structure function  $f_L$  as a function of the deuteron binding energy  $E_B$  for  $q^2 = 0.25 \text{ fm}^{-2}$  and  $p' = 18.6 \text{ MeV}$  at an angle of  $\theta' = 15^\circ$ . The energy  $E'$  is fixed. (Right) The relative influence of the final-state interactions on  $f_L$ .

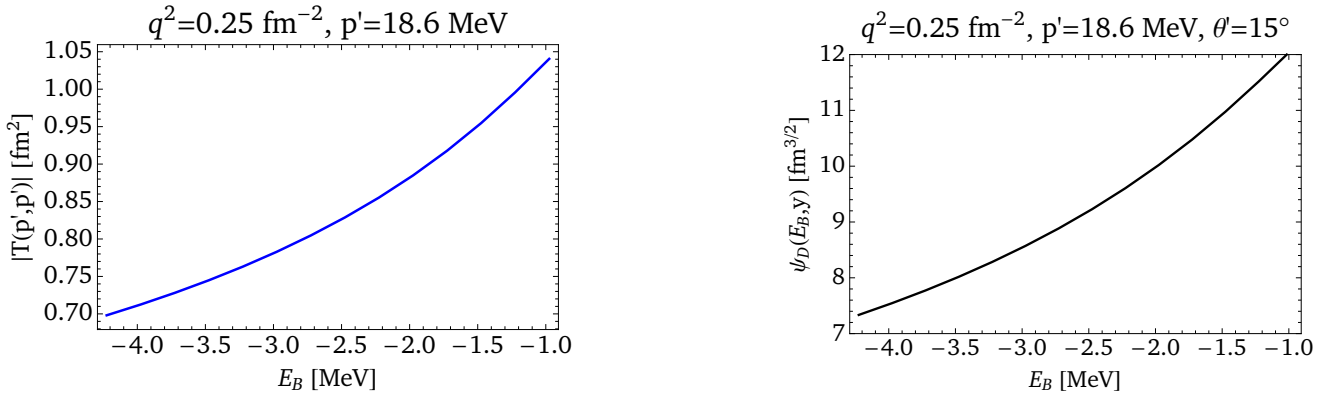


Figure 33: (Left) The absolute value of the on-shell  $T$ -matrix as a function of the deuteron binding energy  $E_B$  at the quasi-free ridge for  $q^2 = 0.25 \text{ fm}^{-2}$  at an angle of  $\theta' = 15^\circ$ . (Right) The deuteron wave function  $\psi_D(E_B, y)$  as a function of the deuteron binding energy for momentum  $y = \sqrt{p'^2 - p' q \cos(\theta')} + q^2/4$ .

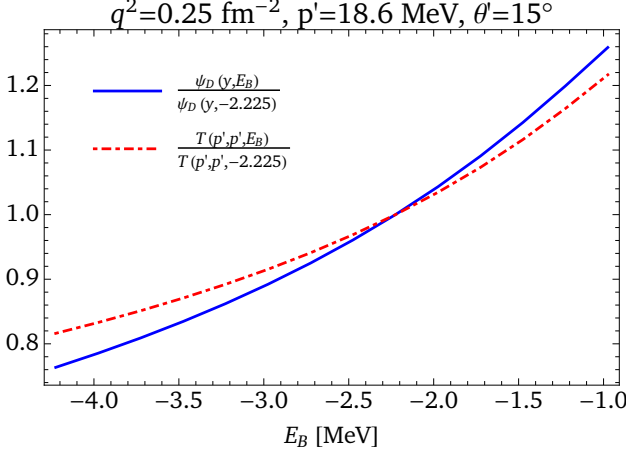


Figure 34: The deuteron wave function and the on-shell  $T$ -matrix for  $q^2 = 0.25 \text{ fm}^{-2}$  and  $p' = 18.6 \text{ MeV}$  as a function of the binding energy  $E_B$  at an angle of  $\theta' = 15^\circ$  normalized to  $E_B = -2.225 \text{ MeV}$ . We find that the deuteron wave function depends stronger on the binding energy and therefore final-state interactions become more important relatively for stronger binding.

approximation becomes increasingly more prominent, leading to the fact that the relative influence of final-state interactions becomes smaller.

This changes at other kinematics. In Fig. 35 we show (left panel)  $f_L$  in the impulse approximation and with included final-state interactions for the same  $q^2$  and  $p'$ , but a different angle  $\theta' = 115^\circ$ ; and (right panel) the ratio  $|f_L^{IA} - f_L^{FSI}|/f_L^{IA}$ . There are two major observations in these plots: first, at a binding energy  $E_B = -1.75 \text{ MeV}$  final-state interactions are negligible, meaning that the  $F_4$  term vanishes. This is what one would have actually expected for  $E_B = -2.225 \text{ MeV}$  if the quasi-free ridge existed in the low-momentum regime. Second, for weak binding final-state interactions dominate the longitudinal structure function in agreement with our expectations stated at the beginning of this section. The reason for the latter observation is that the change of the angle to  $\theta' = 115^\circ$  leads to  $y = 0.3 \text{ fm}^{-1}$ . From Fig. 31 we know that the deuteron wave function hardly changes with the binding energy for  $k > 0.25 \text{ fm}^{-1}$ , whereas the  $T$ -matrix is not at all affected by the angle. Plotting the  $T$ -matrix and the deuteron wave function normalized to the physical binding energy, as done in Fig. 36, we find that the slope of the  $T$ -matrix is larger than the slope of the deuteron wave function for all  $E_B$ . The deuteron wave function

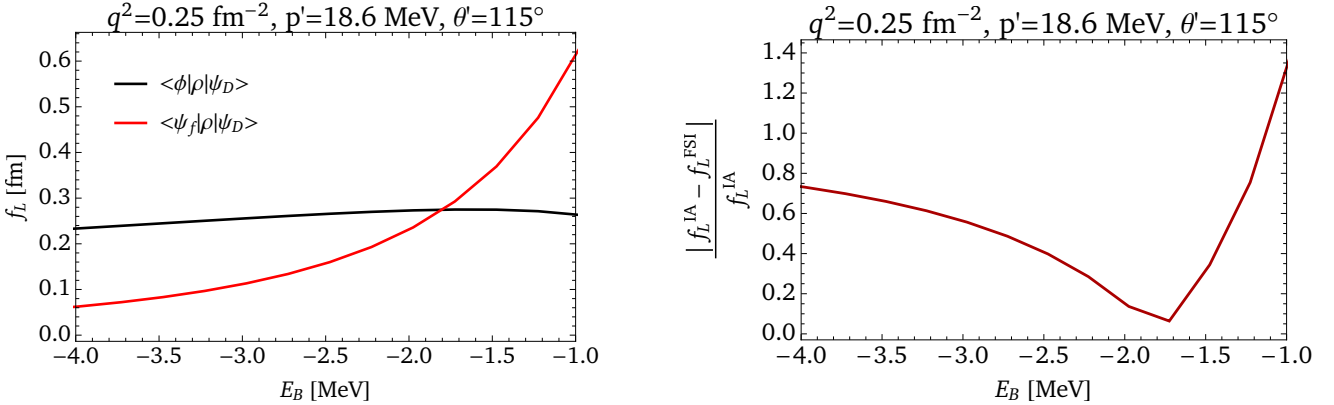


Figure 35: (Left) The longitudinal structure function  $f_L$  as a function of the deuteron binding energy  $E_B$  for  $q^2 = 0.25 \text{ fm}^{-2}$  and  $p' = 18.6 \text{ MeV}$  at an angle of  $\theta' = 115^\circ$ . The energy  $E'$  is fixed. (Right) The relative influence of the final-state interactions on  $f_L$ .

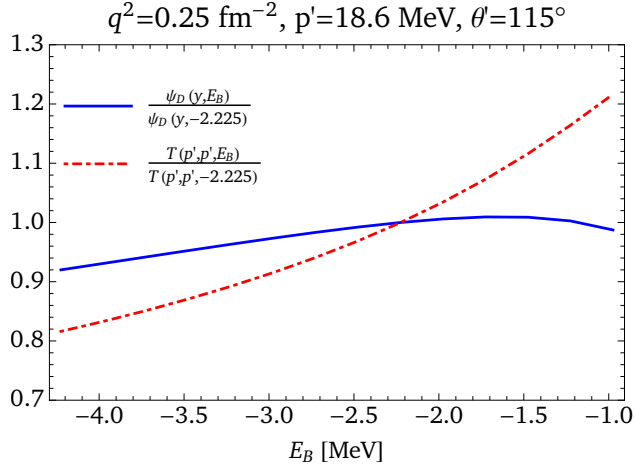


Figure 36: The deuteron wave function and the on-shell  $T$ -matrix for  $q^2 = 0.25 \text{ fm}^{-2}$  and  $p' = 18.6 \text{ MeV}$  as a function of the binding energy  $E_B$  at an angle of  $\theta' = 115^\circ$  normalized to  $E_B = -2.225 \text{ MeV}$ . We find that the deuteron wave function depends less on the binding energy and therefore final-state interactions become less important relatively for stronger binding.

hardly changes over the whole range, and so does  $f_L$  in the impulse approximation. Thus, only final-state interactions are affected by the variation of the binding energy, making them contribute strongly as  $E_B \rightarrow 0$  due to the  $T$ -matrix. In Fig. 37 we show the relative influence of final-state interactions for different angles  $\theta' = 15^\circ$  and  $\theta' = 115^\circ$  as well as for different binding energies  $E_B = -1.225 \text{ MeV}$  and  $E_B = -4.225 \text{ MeV}$ . Note that the results with  $\theta' = 115^\circ$  are at different scales. Both cases show what we would now expect. For  $\theta' = 15^\circ$ , final-state interactions are more prominent for stronger binding due to the deuteron wave function dominating over the  $T$ -matrix. In contrast to that, for  $\theta' = 115^\circ$  final-state interactions can become really large especially for large values of  $q^2$ . What is striking here is that there is a range of kinematics where final state interactions are really small, but it is not at the quasi-free ridge. The relation between photon momentum and nucleon energy there is given by

$$E' (\text{in MeV}) \approx 30q^2 (\text{in fm}^{-2}). \quad (117)$$

This raises the question if Eq. (112) describes the whole quasi-free ridge or if for small energies a different description is necessary. Furthermore, taking into account the angle  $\theta'$  appears to be inevitable in the pionless regime. Investigating this with the Argonne  $v_{18}$  potential or chiral EFT could give rise to this observation.

Our results show that the expectation of the  $T$ -matrix dominating the influence of final-state interactions for weak binding does not hold for all kinematics, but it strongly depends on the argument  $y$  of the wave function. Hence, the unnaturally large scattering length of the  ${}^3S_1$  channel cannot be the only reason why final-state interactions contribute at the quasi-free ridge (given in Eq. (112)) for small momenta because this effect would be enhanced for increased scattering lengths. Investigating this phenomenon will be part of future work.

Comparing Fig. 37 with Fig. 25 confirms what we have already expected: evolution effects and final-state interactions are not correlated in the low-momentum regime. However, in the high-momentum regime they are as shown in Fig. 11.

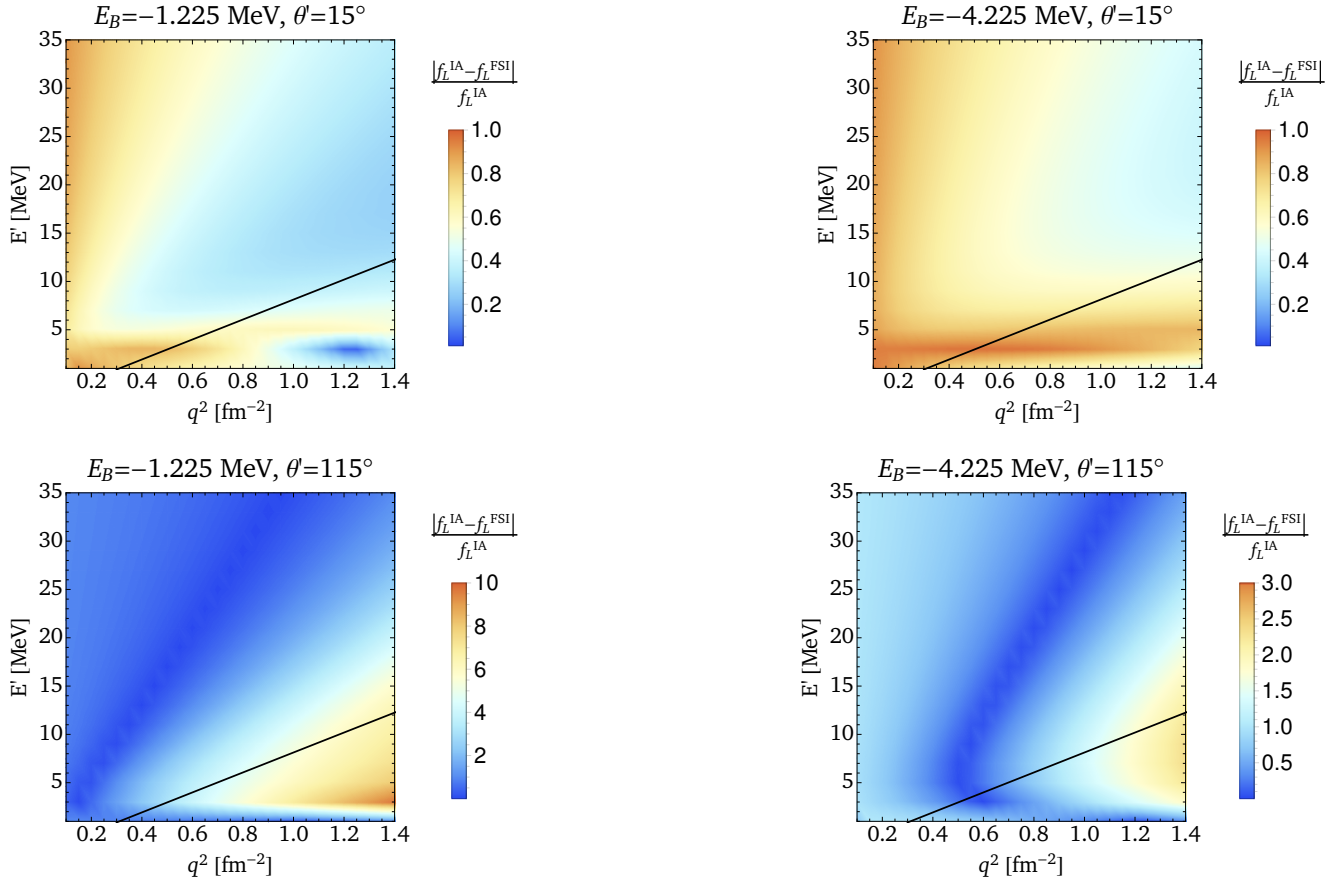


**Figure 37:** The relative influence of final-state interactions for different (top)  $\theta' = 15^\circ$  and (bottom)  $\theta' = 115^\circ$  for the binding energies (left)  $E_B = -1.225$  MeV and (right)  $E_B = -4.225$  MeV. Note that the results with  $\theta' = 115^\circ$  are at different scales. The black solid line symbolizes the quasi-free ridge as given in Eq. (112). We find, in agreement with our analysis, that the angle  $\theta'$  plays a crucial role for the importance of final-state interactions on the longitudinal structure function  $f_L$ . The superscripts "IA" and "FSI" refer to impulse approximation and included final-state interactions, respectively.

---

## 5 Summary and outlook

---

When nuclear Hamiltonians are evolved with SRG methods, not only the potential changes, but operators, initial states, and final-states are affected. The SRG flow equations ensure by construction that observables remain unchanged. However, evolving only some of all relevant quantities results in a violation of this invariance, leading to so-called evolution effects. Investigating these for deuteron electrodisintegration, More et al. [3] found that the evolution effects for the longitudinal structure function  $f_L$ , a quantity directly related to the cross section and therefore an observable, are correlated to the effects of final-state interactions. For some particular regime of kinematic, called the quasi-free ridge, both effects were found to be negligible. An important question that this work set out to investigate was: is the quasi-free ridge really quasi-free for small momenta, and does the correlation of evolution effects and final-state interactions hold in this regime?

In order to investigate the influence of the effects mentioned above on  $f_L$ , the first step was to solve the SRG flow equations for the leading order pionless EFT potential. We found that our potential is very soft by construction. We therefore had to evolve to relatively small values of the decoupling scale  $\lambda$  in order to reach the desired band-diagonal form of the potential shown in Fig. 25. By solving the Schrödinger equation for the unevolved and evolved Hamiltonians  $H$  and  $H_\lambda$ , respectively, done by diagonalization, we obtained the associated deuteron wave functions  $\psi_D$  and  $\psi_D^\lambda$ . Having the evolved potential, we could calculate the smooth part of the transformation matrix  $\tilde{U}$ .

For final state interactions, the  $T$ -matrix, describing the proton and the neutron scattering off each other, is a crucial quantity. We solved the Lippmann-Schwinger equation for the unevolved and evolved potentials  $V$  and  $V_\lambda$ , obtaining the  $T$ -matrices  $T$  and  $T^\lambda$ . Calculating the phase shifts  $\delta(k)$  using the on-shell elements of  $T$  and  $T^\lambda$ , we could confirm that observables remain invariant in the SRG.

With all these ingredients in place, we investigated the influence of final-state interactions in the pionless regime. First of all, we found that pionless EFT is indeed very well suited in order to describe deuteron electrodisintegration in the low-momentum regime. The results for the longitudinal structure function  $f_L$ , calculated using the Argonne  $v_{18}$  potential, fell perfectly inside our uncertainty bands for both impulse approximation and included final-state interactions. We obtained these uncertainty bands by fitting  $C_0$  to the binding energy of the deuteron and the scattering length  $a_T$  of the  $^3S_1$  channel, leading to the expected influence of roughly 30%. In addition to that, we found that final-state interactions are very important for small momenta, even at the quasi-free ridge. Our hypothesis for this observation was that it is due to the on-shell element of the  $T$ -matrix  $T(p', p')$  which is directly related to the unnaturally large scattering length  $a_T = 5.4 \text{ fm}^{-1}$ . In order to test this hypothesis, we varied the binding energy of the deuteron to stronger and weaker binding, resulting in a larger and smaller scattering length, respectively. One major advantage of pionless EFT is that this variation can be done very easily. We found that a larger scattering length does not necessarily lead to more important final-state interactions, in contradiction to our hypothesis. This is due to the deuteron wave function which depends strongly on the binding energy in the low-momentum area for  $k < 0.25 \text{ fm}^{-1}$ . Hence, the relevance of final-state interactions strongly depends on the argument  $y$  of the deuteron wave function and therefore especially on the angle  $\theta'$ . While for  $\theta' = 15^\circ$  final-state interactions become more important with stronger binding, for  $\theta' = 115^\circ$  their relevance decreases. A very striking observation in the latter case was the existence of a range of kinematics where final-state interactions are small. However, this is not at the quasi-free ridge, but at some different kinematical composition roughly given by  $E'$  (in MeV)  $\approx 30q^2$  (in  $\text{fm}^{-2}$ ).

Investigating final-state interactions beyond the pionless regime, we found that the Argonne  $v_{18}$  results did not fall within our uncertainty bands. However, our results showed that pionless EFT is very well suited to qualitatively describe physics beyond its regime. We were especially able to reproduce Fig. 11 from More et al. [3], showing that final-state interactions are small at the quasi-free ridge for photon momenta  $q^2 > 4 \text{ fm}^{-2}$ .

Regarding evolution effects beyond the pionless regime, we found that they are not negligible at the quasi-free ridge, but their strength increases for larger  $q^2$ . This result is in contradiction to what we would

---

have expected from the correlation of final-state interactions and evolution effects. Within the pionless regime however, evolution effects are almost negligible at the quasi-free ridge and become increasingly stronger as one moves to different kinematics. Hence, we could perfectly reproduce the expectations of small evolution effects at the quasi-free ridge in this regime as shown in Fig. 25.

Considering the questions stated above, we can now give the following answers: the correlation of final-state interactions and evolution effects does not hold in the pionless regime. While evolution effects behave as expected, i.e., they are small at the quasi-free ridge, final-state interactions contribute strongly at this kinematic. This is partly due to the on-shell  $T$ -matrix which is large for low momenta because of the connection to the scattering length. However, we found that there has to be some further contribution because enlarging the scattering length did not necessarily lead to stronger final-state interactions.

In future work it would be very interesting to further investigate our observations. Finding the same results using some different potential would not only confirm the applicability of pionless EFT but it would also proof that the correlation of evolution effects and final-state interactions does not exist in the low-momentum regime. Furthermore, an investigation of the importance of final-state interactions in the pionless regime is necessary, especially regarding the angular dependence and the range of kinematics where final-state interactions were actually small. If our observations were also confirmed using for example chiral EFT, one would have to consider a different formulation of the quasi-free ridge in the low-momentum area.

## 6 Appendix

### 6.1 Matrix products

In Sec. 2.4.1 we list some of the important matrix products that occur in our calculations. Here, we show the remaining products and give some details on how to calculate them. We start with the evolved wave function, which can be calculated by acting with the transformation matrix on the unevolved wave function and inserting an identity as shown in Eq. (90). We then get

$$\begin{aligned}\langle k_i | \psi_s \rangle &= \langle k_i | U_s | \psi_0 \rangle \\ &= \frac{2}{\pi} \sum_n w_n q_n^2 U_s(k_i, k_n) \psi_0(k_n).\end{aligned}\quad (118)$$

The evolution of the Hamiltonian is the central part of the SRG evolution. Although the evolved Hamiltonian is obtained by Eq. (94), we here want to show the alternative way via the transformation matrices  $U_s$ . Using Eq. (16) and inserting three identities, we find

$$\begin{aligned}\langle k_i | H_s | \psi_s \rangle &= \langle k_i | U_s H_0 U_s^\dagger | \psi_s \rangle \\ &= \frac{4}{M\pi^2} \sum_{j,l} w_j k_j^4 U_s(k_i, k_j) w_l k_l^2 U^\dagger(k_j, k_l) \psi_s(k_l) \\ &\quad + \frac{8}{\pi^3} \sum_{j,k,l} w_j k_j^2 U_s(k_i, k_j) w_k k_k^2 V(k_j, k_k) w_l k_l^2 U^\dagger(k_j, k_l) \psi_s(k_l),\end{aligned}\quad (119)$$

where we used  $H_0 = T + V$ . Since an operator is evolved just like the Hamiltonian, we find that the evolution of the one-body current leads to

$$\begin{aligned}\langle k_i | \rho_s(\mathbf{q}) | k_j \rangle &= \langle k_i | U_s \rho(\mathbf{q}) U_s^\dagger | k_j \rangle \\ &= \frac{4}{\pi^2} \sum_{n,m} w_n k_n^2 U_s(k_i, k_n) w_m k_m^2 \rho(k_n, k_m) U_s^\dagger(k_m, k_j).\end{aligned}\quad (120)$$

It is possible to symmetrize the matrices. Instead of multiplying the Gauss-Legendre quadrature nodes and weights only in columns, it is possible to define

$$\tilde{V}_{ij} = \sqrt{\frac{2}{\pi}} \sqrt{w_i} k_i V_{ij} k_j \sqrt{w_j}, \quad (121)$$

where  $V_{ij}$  are matrix elements of the initial potential. With this choice, nodes and weights are included directly in the matrices, so it is possible to calculate matrix products directly. However, observables are independent of this choice. That is why we choose the for us more intuitive definition.

---

## Acknowledgement

---

First of all, I want to thank Achim Schwenk for giving me the opportunity to do this work at his group. I am very grateful to Sebastian König for supporting me during this work and always having an idea on how to fix problems and how to test results.

I want to thank the members of our office for helpful discussions as well as all the members of the Strongint group for a nice and funny time. Here, I want to especially thank Jan Hoppe who not only proofread parts of this thesis but with whom I shared a very good time.

Last but not least, I want to thank my family and my girlfriend for their support.

---

## References

---

- [1] U. van Kolck, Nucl. Phys. A **645**, 273 (1999).
  - [2] E. Jurgenson, *Applications of the Similarity Renormalization Group to the Nuclear Interaction*, Ph.D. thesis, The Ohio State University (2008).
  - [3] S. N. More, S. König, R. J. Furnstahl, and K. Hebeler, Phys. Rev. C **92**, 064002 (2015).
  - [4] S. N. More, S. K. Bogner, and R. J. Furnstahl, Phys. Rev. C **96**, 054004 (2017).
  - [5] H. Arenhövel, W. Leidemann, and E. L. Tomusiak, Few Body Syst. **28**, 147 (2000).
  - [6] P. von Neumann-Cosel, A. Richter, G. Schrieder, A. Shevchenko, A. Stiller, and H. Arenhövel, Phys. Rev. Lett. **88**, 202304 (2002).
  - [7] S. Christlmeier and H. W. Griesshammer, Phys. Rev. C **77**, 064001 (2008).
  - [8] S. Weinberg, Physica A **96**, 327 (1979).
  - [9] E. Epelbaum (2010) 1001.3229 .
  - [10] M. Schönborn, *Relativistische Boost-Korrekturen der führenden Wechselwirkungen in chiraler effektiver Feldtheorie*, Bachelor's thesis, Technische Universität Darmstadt (2016).
  - [11] E. Epelbaum, H.-W. Hammer, and U.-G. Meißner, Rev. Mod. Phys. **81**, 1773 (2009).
  - [12] H.-W. Hammer and R. J. Furnstahl, Nucl. Phys. A **678**, 277 (2000).
  - [13] J. Vanasse, (2017), 1706.02665 .
  - [14] S. König, J. Phys. G **44**, 064007 (2017).
  - [15] J.-W. Chen and M. J. Savage, Phys. Rev. C **60**, 065205 (1999).
  - [16] P. F. Bedaque and U. van Kolck, Phys. Lett. B **428**, 221 (1998).
  - [17] S. König, *Effective quantum theories with short- and long-range forces*, Ph.D. thesis, Rheinische Friedrich-Wilhelms-Universität Bonn (2013).
  - [18] K. G. Wilson, Phys. Rev. B **4**, 3174 (1971).
  - [19] K. G. Wilson, Phys. Rev. D **3**, 1818 (1971).
  - [20] K. G. Wilson, Phys. Rev. B **4**, 3184 (1971).
  - [21] S. D. Glazek and K. G. Wilson, Phys. Rev. D **48**, 5863 (1993).
  - [22] S. D. Glazek and K. G. Wilson, Phys. Rev. D **49**, 4214 (1994).
  - [23] F. Wegner, Ann. Phys. **506**, 77 (1994).
  - [24] S. Szpigiel and R. J. Perry, , 59 (2000).
  - [25] R. J. Furnstahl, Nucl. Phys. Proc. Suppl. **228**, 139 (2012).
  - [26] K. Hebeler and R. J. Furnstahl, Phys. Rev. C **87**, 031302 (2013).
  - [27] S. K. Bogner, R. J. Furnstahl, and R. J. Perry, Phys. Rev. C **75**, 061001(R) (2007).
-

- 
- [28] E. Anderson, S. K. Bogner, R. J. Furnstahl, E. D. Jurgenson, R. J. Perry, and A. Schwenk, Phys. Rev. C **77**, 037001 (2008).
- [29] R. J. Furnstahl and K. Hebeler, Rep. Prog. Phys. **76**, 126301 (2013).
- [30] N. M. Dicaire, C. Omand, and P. Navrátil, Phys. Rev. C **90**, 034302 (2014).
- [31] H. Hergert, S. K. Bogner, S. Binder, A. Calci, J. Langhammer, R. Roth, and A. Schwenk, Phys. Rev. C **87**, 034307 (2013).
- [32] S. K. Bogner, R. J. Furnstahl, and A. Schwenk, Prog. Part. Nucl. Phys. **65**, 94 (2010).
- [33] E. D. Jurgenson, P. Navrátil, and R. J. Furnstahl, Phys. Rev. Lett. **103**, 082501 (2009).
- [34] W. Li, E. R. Anderson, and R. J. Furnstahl, Phys. Rev. C **84**, 054002 (2011).
- [35] E. R. Anderson, S. K. Bogner, R. J. Furnstahl, and R. J. Perry, Phys. Rev. C **82**, 054001 (2010).
- [36] J. Simonis, *Ab-Initio calculations of nuclei using chiral interactions with realistic saturation properties*, Ph.D. thesis, Technische Universität Darmstadt (2017).
- [37] K. A. Wendt, Phys. Rev. C **87**, 061001(R) (2013).
- [38] T. W. Donnelly and A. S. Raskin, Annals Phys. **169**, 247 (1986).
- [39] C. J. Yang and D. R. Phillips, Eur. Phys. J. A **49**, 122 (2013).
- [40] A. S. Raskin and T. W. Donnelly, Annals Phys. **191**, 78 (1989).
- [41] R. H. Landau, *Quantum Mechanics II: A Second Course in Quantum Theory*, 2nd ed. (John Wiley and Sons, 1995).
- [42] V. Lensky, M. C. Birse, and N. R. Walet, Phys. Rev. C **94**, 034003 (2016).
- [43] S. König, *Coulomb effects in pionless effective field theory*, Master's thesis, Rheinische Friedrich-Wilhelms-Universität Bonn (2010).
- [44] W. Glöckle, G. Hasberg, and A. R. Negehabian, Z. Phys. A **305**, 217 (1982).